JGR Solid Earth

RESEARCH ARTICLE
10.1029/2023JB026688

A New Shear-Velocity Model of Continental Australia Based on Multi-Scale Surface-Wave Tomography

Fabrizio Magrini[1,2], Emanuel Kästle[3], Simone Pilia[4], Nicholas Rawlinson[5], and Luca De Siena[1]

[1]Institute of Geosciences, Johannes Gutenberg University, Mainz, Germany, [2]Research School of Earth Sciences, The Australian National University, Canberra, ACT, Australia, [3]Institute for Geological Sciences, Freie Universität, Berlin, Germany, [4]College of Petroleum Engineering and Geosciences, King Fahd University of Petroleum and Minerals, Dhahran, SA, USA, [5]Department of Earth Sciences-Bullard Labs, University of Cambridge, Cambridge, UK

Abstract The Australian Seismological Reference Model (AuSREM) represents a state-of-the-art geophysical synthesis of the Australian continent. To date, its shear-wave component has limited resolution at lower-crustal to uppermost-mantle depths, where it is mainly constrained by sparse measurements collected at the local scale. In this study, we compile a large data set of surface-wave phase velocities based on seismic ambient noise and teleseismic earthquakes, to produce Rayleigh and Love phase-velocity maps of continental Australia in a broad period range (4–200 s). Via transdimensional Bayesian inversion, we translate the phase-velocity maps into a 3-D shear-wave velocity model extending to 300 km depth. Owing to the unprecedented seismic coverage and to the joint use of ambient-noise and teleseismic data, the retrieved model fills a tomographic gap in the known shear-wave velocity structure of the continent, comprising lower-crustal to uppermost mantle depths. Consistent with AuSREM, strong velocity heterogeneities in our model highlight the (faster) cratonic blocks and the (slower) sedimentary basins at upper-crustal depths. At mantle depths, the most prominent feature of the continent is a large-scale eastward decrease in shear-wave velocity. We interpret our observations in light of the relevant literature, and produce depth maps of the Moho and lithosphere-asthenosphere boundary (LAB). Notably, our LAB proxy features a stripe of thicker lithosphere extending to the east coast, which is not visible in the AuSREM LAB model. This observation supports the idea that lateral variations in lithospheric thickness control both the composition and volume of surface volcanism in eastern Australia.

Plain Language Summary The current seismological reference model of Australia (AuSREM) provides spatial variations in compressional- and shear-wave velocity, but has limited resolution at lower-crustal to uppermost-mantle depths. In this study, we measure surface-wave (Rayleigh and Love) phase velocities across Australia using both seismic ambient noise (continuous background noise largely generated by oceans) and teleseismic (distant) earthquakes. We use the compiled data set to produce a 3-D shear-wave velocity model of Australia, characterized by unprecedented resolution throughout the crust and extending to 300 km depth. Consistent with AuSREM, our model allows the (faster) cratonic blocks to be clearly discriminated from the (slower) sedimentary basins at upper-crustal depths. The upper mantle beneath Australia is characterized by a large-scale pattern of shear-wave velocity decreasing eastward. Through our 3-D shear-wave velocity model, we also provide estimates of crustal and lithospheric thickness. The lateral variations of the latter support the hypothesis that lithospheric thickness controls both the composition and volume of surface volcanism in eastern Australia.

Key Points:

- 3-D shear-velocity model of Australia extending to 300 km depth, derived from Rayleigh and Love phase velocities in the period range 4–200 s
- Continent-wide estimate of Moho, and good illumination of structural continuity between lower crust and upper mantle
- Lithosphere-asthenosphere boundary proxy supports lithospheric thickness controlling the composition and volume of surface volcanism in eastern Australia

Supporting Information:

Supporting Information may be found in the online version of this article.

Correspondence to:

F. Magrini,
fmagrini@uni-mainz.de

Citation:

Magrini, F., Kästle, E., Pilia, S., Rawlinson, N., & De Siena, L. (2023). A new shear-velocity model of continental Australia based on multi-scale surface-wave tomography. *Journal of Geophysical Research: Solid Earth*, *128*, e2023JB026688. https://doi.org/10.1029/2023JB026688

Received 8 MAR 2023
Accepted 6 JUN 2023

Author Contributions:

Methodology: Fabrizio Magrini
Software: Emanuel Kästle
Writing – original draft: Fabrizio Magrini, Emanuel Kästle, Simone Pilia, Nicholas Rawlinson, Luca De Siena

1. Introduction

The ancient, weathered Australian continent features one of the most limited outcrops of bedrock geology worldwide. Tectonic activity is much lower than in any other continent except Antarctica, with few known active faults especially around its cratonic cores (Blewett, 2012). Geophysics, particularly seismic imaging, has thus been the primary source of information on the subsurface at both crustal and upper-mantle scales (Kennett et al., 2013, 2018). Portable and permanent seismic arrays have covered much of the continent through the last three decades (Rawlinson et al., 2014; van der Hilst et al., 1994), providing data for continent-wide tomographic imaging. While earthquakes are widespread, they are primarily found at the continent boundaries and (to a much lesser extent) the Flinders Ranges (Kennett et al., 2018), where they offer sufficient information to obtain highly resolved images of the crust and mantle (e.g., Pilia et al., 2013). Teleseismic tomography (e.g., Rawlinson

et al., 2006; Rawlinson & Kennett, 2008) and ambient-noise-based approaches (Saygin & Kennett, 2010, 2012; Young et al., 2013) are excellent alternatives to image the rest of the continent.

At the time of writing, the Australian Seismological Reference Model (AuSREM) represents the most detailed 3-D model of Australia, encompassing nationwide seismological information on both its crust (Salmon et al., 2013) and mantle (Kennett et al., 2013, 2018; Sun & Kennett, 2016; Yoshizawa, 2014; Yoshizawa & Kennett, 2015). Provided at a pixel dimension of 0.5° × 0.5°, AuSREM is not the result of a joint inversion of seismic observables; rather it is an assemblage of seismic properties retrieved from refraction and reflection profiles, receiver functions, and tomographic studies performed at different scales throughout the continent. As a consequence, the spatial resolution of AuSREM varies substantially with location and depth, depending on the data coverage and methods originally employed to derive its individual parts (see Kennett et al., 2018, and citations therein).

While the deeper ($\gtrsim$75 km depth) portion of AuSREM can be considered relatively robust (Kennett et al., 2018), since it is constrained by a large number of independent earthquake-based studies, its shallower regions remain less resolved. In fact, AuSREM's S-wave crustal component has primarily been derived from the 3-D shear-velocity model of Saygin and Kennett (2012); this model exploited coverage and imaging techniques available more than a decade ago, and displays only limited correlation with the shallow sedimentary cover and surface tectonic features. Moreover, the model of Saygin and Kennett (2012) relied on surface-wave group velocities, known to have smaller sensitivity to deep structures compared to phase velocities (e.g., Smith et al., 2004), and its reliability quickly decreases at depths greater than 25 km (Salmon et al., 2013). For this reason, the shear-wave velocity structure of a large portion of the lower Australian crust has mainly been interpolated/extrapolated/converted from refraction and receiver-function results (see Figure 7.15 in Kennett et al., 2018), to overcome the sparsity of receivers characterizing the central part of the continent.

This study aims to provide an improved shear-wave velocity model of the Australian crust and upper mantle at the continental scale, including estimates of Moho and lithosphere-asthenosphere boundary depth. To this end, we join surface-wave phase-velocity measurements obtained from both teleseismic earthquakes and seismic ambient noise, and exploit all available seismic records to maximize data coverage across the continent. In general, ambient-noise and earthquake data have complementary sensitivity. When used jointly, they provide well resolved images at the lithospheric scale and high-resolution models of the crust where data coverage is sufficient (e.g., Kästle et al., 2018; Magrini, Diaferia, et al., 2022; Rawlinson et al., 2016; Yang et al., 2008; Zhou et al., 2012).

After providing a brief overview of the geology and tectonic setting of Australia (Section 2), we explain in Section 3 how we calculated Rayleigh and Love phase velocities between pairs of receivers, based on teleseismic earthquakes and seismic ambient noise. Section 4 concerns the calculation of phase-velocity maps at different surface-wave periods, which we carried out by means of adaptive parameterizations to enhance the resolution across Australia. The inversion of the subsequent Rayleigh and Love phase-velocity maps for shear-wave velocity, performed through a state-of-the-art Bayesian inversion scheme, is explained in Section 5. A detailed discussion of our model is presented in Section 6.

2. Tectonic and Geological Setting

The geological history of the Australian continent can be traced back to the very early stages of our planet's existence, with evidence suggesting that parts of the continental lithosphere were formed up to ~4.4 billion years ago (Harrison et al., 2005; Valley et al., 2014). Australia incorporates three very ancient cratonic blocks (often referred to as West, South and North Australian Cratons) that survived Proterozoic and Phanerozoic tectonism, including the assemblage and breakup of different supercontinents. Additional lithospheric fragments were joined together by slab collisions, lithospheric extensions, accretionary and volcanic events to create the present day architecture of the continent (for a review see, e.g., Betts et al., 2002).

2.1. Archean-Proterozoic Australia

Western Australia comprises some of the most ancient terranes on Earth (Figure 1a). Among them is the Yilgarn Craton, which formed ~3.73–2.55 Ga and hosts zircon crystals as old as 4.374 Ga (Valley et al., 2014). Around 2.2–1.6 Ga, the Yilgarn Craton collided with the Pilbara Craton (formed ~3.65–2.00 Ga) to establish the wider West Australian Craton (Barley et al., 1998; Betts et al., 2002; Cawood & Tyler, 2004; Myers et al., 1996).

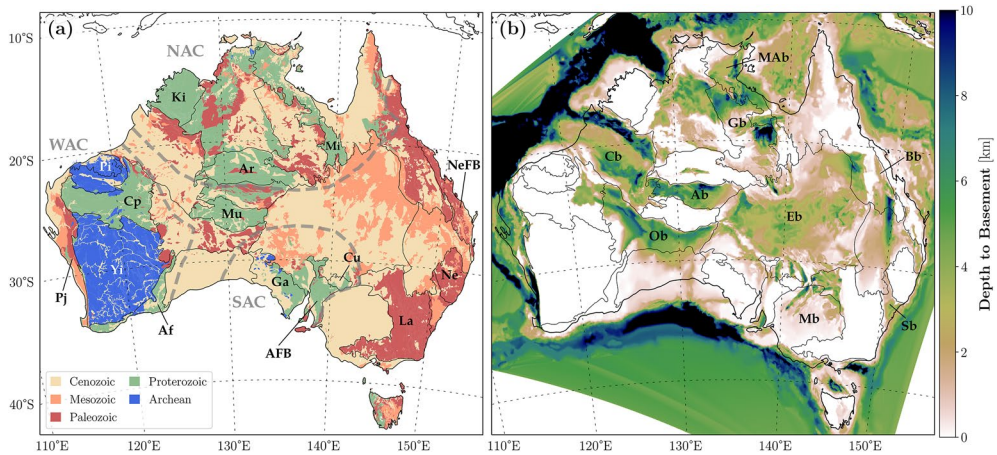

Figure 1. Major geologic units as visible at the surface (a) and sedimentary thickness based on the OZ SEEBASE® 2021 model (b) of continental Australia. The dashed gray lines outline the North (NAC), South (SAC), and West (WAC) Australian Cratons. Boundaries between different geologic units were drawn after Blewett (2012). Key to marked features: Amadeus Basin (Ab), Albany-Fraser Orogen (Af), Adelaide Fold Belt (AFB), Arunta Province (Ar), Bowen Basin (Bb), Canning Basin (Cb), Capricorn Orogen (Cp), Curnamona Province (Cu), Eromanga Basin (Eb), Gawler Craton (Ga), Georgina Basin (Gb), Kimberley Block (Ki), Lachlan Orogen (La), McArthur Basin (MAb), Murray Basin (Mb), Mt Isa Province (Mi), Musgrave Province (Mu), New England Orogen (Ne), New England Fold Belt (NeFB), Officer Basin (Ob), Pilbara Craton (Pi), Pinjarra Orogen (Pj), Sydney Basin (Sb), Yilgarn Craton (Yi).

This collision resulted in the Capricorn Orogen, which has been the site of repeated deformation and metamorphism during several orogenies: the Ophthalmian (~2,200 Ma), the Glenburgh (2,000-1,960 Ma), the Capricorn (1,830-1,780 Ma), and an unnamed event at the end of the Palaeoproterozoic (~1,670-1,620 Ma) (Betts & Giles, 2006; Cawood & Tyler, 2004).

The South Australian Craton consists of the amalgamation of the Archean-to-Mesoproterozoic Gawler Craton to the west and the Paleoproterozoic Curnamona Province to the east. Proterozoic and Mesozoic sediments mask most of its structure (Figure 1b). The North Australian Craton comprises several blocks of Precambrian age, including the Kimberly Craton, Mt Isa Province, and Arunta Province (Betts et al., 2002). Similarities between some portions of the South and North Australian Cratons (e.g., between Mt Isa and both the Curnamona Province and the northern Gawler Craton, and the Arunta Province and the Gawler Craton; Giles et al., 2004; Betts & Giles, 2006) suggest that, prior to ~1,450 Ma, they were part of a greater proto-Australian continent. Later events are thought to have first separated these two large parts of the continent and then eventually re-amalgamated them, together with the West Australian Craton, during the 1330-1100 Ma Albany-Fraser and Musgrave orogenies. The South Australian Craton is now separated from the North Australian Craton by the Proterozoic Musgrave Block and several Phanerozoic sedimentary basins (Wade et al., 2008).

The tectonic activity (1,300–1,000 Ma) that brought about this confluence of terranes was also responsible, at a larger scale, for assembling the Meso-Neoproterozoic supercontinent Rodinia, of which Precambrian Australia was a part (Li et al., 2008; Myers et al., 1996). The intracratonic basins in the continental interior developed after a regional hiatus (~1,100-830 Ma) preceded by a period of intracratonic basin development (Walter et al., 1995); this led to the Neoproterozoic fill of the Amadeus, Georgina, and Officer Basins (de Vries et al., 2008). The Neoproterozoic-to-Cambrian thick sedimentary package known as the Adelaide Rift Complex (de Vries et al., 2008) (or Adelaide Fold Belt, Preiss, 2000) formed during the breakup of the Rodinia supercontinent due to continental rifting and shortening, the exact timing and locus of which remains debated (Direen and Crawford, 2003b, 2003a; Li et al., 2008; Powell et al., 1993; Wingate et al., 1998; Wingate & Giddings, 2000).

During this period of intense deformation, northeast-southwest compression followed by northeast-southwest extension was concentrated on the Adelaide Rift Complex (Betts et al., 2002). Until the earliest Cambrian, Australia then mostly underwent extension along the eastern margin of its Precambrian core (Foster & Gray, 2000), with major folding and thrusting as a result of suture reactivation between the three main cratonic blocks (~620-540 Ma).

2.2. Phanerozoic Australia

Between ~550-530 Ma Australia amalgamated with other continents, leading to the final formation of Gondwana (Li et al., 2008; Meert, 2001). Evidence of such an amalgamation can be found in the so-called "Tasmanides," a sequence of orogenic belts partly outcropping in Eastern Australia that were constructed via subduction-accretion of the proto-Pacific slab (for a recent review, see Rosenbaum, 2018). The Tasman Orogeny essentially reflects the tectonic unrest that led to the formation of Pangaea through the collision of Gondwana and Laurussia (~320–330 Ma). The orogen eventually ceased with the breakup of Gondwana-Pangaea (~227 Ma, Glen et al., 2005), although some argue that its evolution is still ongoing (Glen & Meffre, 2009). The major terranes in southeast Australia include, from west to east, the Delamerian Orogen and the Lachlan Orogen. Further north, the Thomson Orogen lies between the Delamerian and the north-south trending Bowen, Surat, and Sydney basins, east of which is the New England Orogen (Glen, 2013). The northeastern tip of the Tasmanides comprises the Mossman Orogen.

Extensive Phanerozoic sediment infills such as the Eromanga basin cover large portions of the Tasmanides, concealing the Thomson, Lachlan, and Mossman Orogens (Kennett et al., 2018; Spampinato et al., 2015). Despite the significant hydrocarbon potential, extended seismic surveys of these basins are rare and sediment thickness has primarily been mapped by magnetic and gravity studies, with additional control from water bores, surface mapping, and satellite imagery (Cowley, 2020). For example, high-amplitude magnetic anomalies in the north-eastern and central eastern portion of the Eromanga Basin are believed to be associated with Lower Palaeozoic volcanic products, a consequence of extensive Proterozoic volcanic activity across the Gawler craton (Kennett et al., 2018). Older sediments across northern and central Australia have different characteristics from those across the Tasmanides, as inferred from previous seismological investigations (Salmon et al., 2013; Saygin & Kennett, 2012).

In summary, Australia comprises an amalgamation of three Archean-to-Proterozoic cratonic blocks that characterize the western part of the continent, bounded to the east by different Phanerozoic units that were largely formed through a process of subduction-accretion along the eastern proto-Pacific margin of Gondwana (Glen et al., 2005; Gray & Foster, 2004; Kennett et al., 2004). A significant portion of these lithospheric units lie hidden under the extended Proterozoic-to-Phanerozoic sedimentary cover. Across the Neoproterozoic Adelaide Fold Belt and Paleozoic Lachlan Fold Belt, there is evidence of ongoing active deformation, including Quaternary fault displacement, testifying that the Australian continent is not entirely quiescent (Braun et al., 2009; Pilia et al., 2013; Sandiford et al., 2003).

3. Rayleigh and Love Phase Velocities

We extract fundamental-mode Rayleigh and Love phase velocities beneath the Australian continent from both seismic ambient noise and teleseismic earthquakes. All data processing—from the download of seismograms and calculation of inter-station dispersion curves (Sections 3.1 and 3.2) to their inversion for phase-velocity maps (Section 4)—was carried out in an automated fashion, using the SeisLib Python library (Magrini, Lauro, et al., 2022). In the following sections, to make this manuscript as self-contained but as focussed as possible, we summarize the algorithmic aspects that were most relevant to our work. Further technical details can be found in Magrini, Lauro, et al. (2022).

3.1. Seismic Ambient Noise

We download three-component seismograms recorded between June 1991 and January 2022 at 1,169 different receivers distributed across the study area (Figure 2). We pre-process each seismogram so as to remove mean and linear trends, taper (5%), bandpass filter between 0.01 and 0.5 Hz, and deconvolve with the instrument response to get displacement. We merge the recordings from each receiver into continuous time series, and use zero-padding to fill any temporal gaps.

We use the pre-processed seismic data to measure Rayleigh and Love phase velocity via a four-step procedure; (a) we identify pairs of receivers for which at least 15 days of simultaneous recordings are available. (b) For each of these pairs, we subdivide their recordings into hour-long overlapping (50%, Seats et al., 2012) time-windows, and cross-correlate them in the frequency domain (cross-correlation is performed on the vertical component to

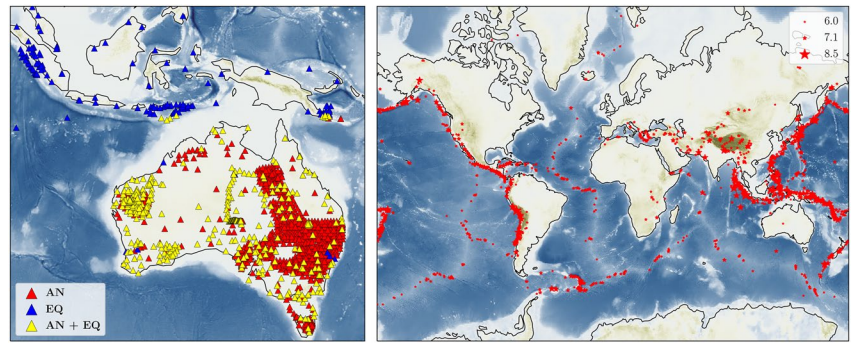

Figure 2. Left: location of the 1,332 different seismometers used to measure Rayleigh and Love phase velocities from seismic ambient noise (AN, Section 3.1) and teleseismic earthquakes (EQ, Section 3.2). The yellow triangles refer to the receivers for which both AN and EQ dispersion curves were retrieved. Right: epicenters (red stars, scaled according to magnitude) of the 2,378 earthquakes employed in the analysis.

measure Rayleigh-wave phase velocities, on transverse components for Love-wave velocity). (c) We then ensemble average the resultant cross-correlations to obtain a unique cross-spectrum. (d) Finally, we extract an average inter-station dispersion curve (Figures 3a and 3c); to do so, SeisLib relies on the experimental assumptions that the ambient seismic noise is diffuse and surface-wave attenuation is sufficiently small to only affect the amplitude of the cross-spectrum (and not its phase, e.g., Boschi & Weemstra, 2015; Magrini & Boschi, 2021). In practice, plausible values of phase velocity are first identified at discrete frequencies corresponding to the zero-crossings of the zeroth order Bessel function of the first kind associated with the receiver pair under consideration (e.g., Ekström et al., 2009; Kästle et al., 2016). The resulting velocity ambiguity (Figures 3a and 3c) is then overcome with the aid of a reference curve (Magrini, Lauro, et al., 2022).

Overall, the above procedure retrieves 25,196 Rayleigh- and 19,041 Love-wave dispersion curves, spanning surface-wave periods between 3 and 50 s. Examples of these curves, together with some information on the collected data set, are illustrated in Figure 3. The length of the seismic traces employed in the cross-correlations is shown, in the form of histograms, in the supplementary material associated with this paper (Figure S1 in Supporting Information S1).

3.2. Teleseismic Earthquakes

We measure Rayleigh and Love phase velocities from waveforms generated by distant earthquakes using a two-station method (e.g., Magrini et al., 2020; Meier et al., 2004). The two-station method assumes that teleseismic surface waves can be decomposed into monochromatics (e.g., Ekström et al., 1997), and considers epicenters approximately aligned on the same great-circle path as target receiver pairs. As the wavefront propagates between the two seismometers, it undergoes a phase shift ϕ depending on inter-station distance Δ and average velocity of propagation c. In the frequency domain, measurements of surface-wave phase velocity can then be retrieved through the dispersion relation

$$c(\omega) = \frac{\omega\Delta}{\phi(\omega) + 2n\pi}, \tag{1}$$

where ω denotes angular frequency and n is an integer. Similar to the previous section (compare Figures 3a and 3c with Figures 3b and 3d), the invariance of ϕ under 2π translations makes it necessary to overcome a phase-velocity ambiguity (e.g., Magrini, Lauro, et al., 2022; Soomro et al., 2016).

We apply this method to three-component recordings of strong (magnitudes between 6 and 8.5) and shallow (<50 km) earthquakes from 577 receivers deployed across South-East Asia and Australia (Figure 2). For each receiver, we download teleseismic-earthquake data from January 2001 to September 2021, selecting epicentral distances between 20° and 140°. We demean, detrend, taper (5%), and bandpass filter each seismogram between 0.005 and 0.1 Hz. We convert the downloaded seismograms to displacement and resample to 1 Hz.

Overall, we find 2,378 earthquakes satisfying the above criteria (Figure 2), and use them to retrieve Rayleigh and Love dispersion curves through the automated algorithm provided by SeisLib; this involves the following. (a) We first identify triplets of epicenters-receivers (one earthquake and two receivers per triplet) that approximately lie on the same great-circle path (we allow for maximum azimuthal deviations of 7.5°). In total, we find 8,519 receiver pairs

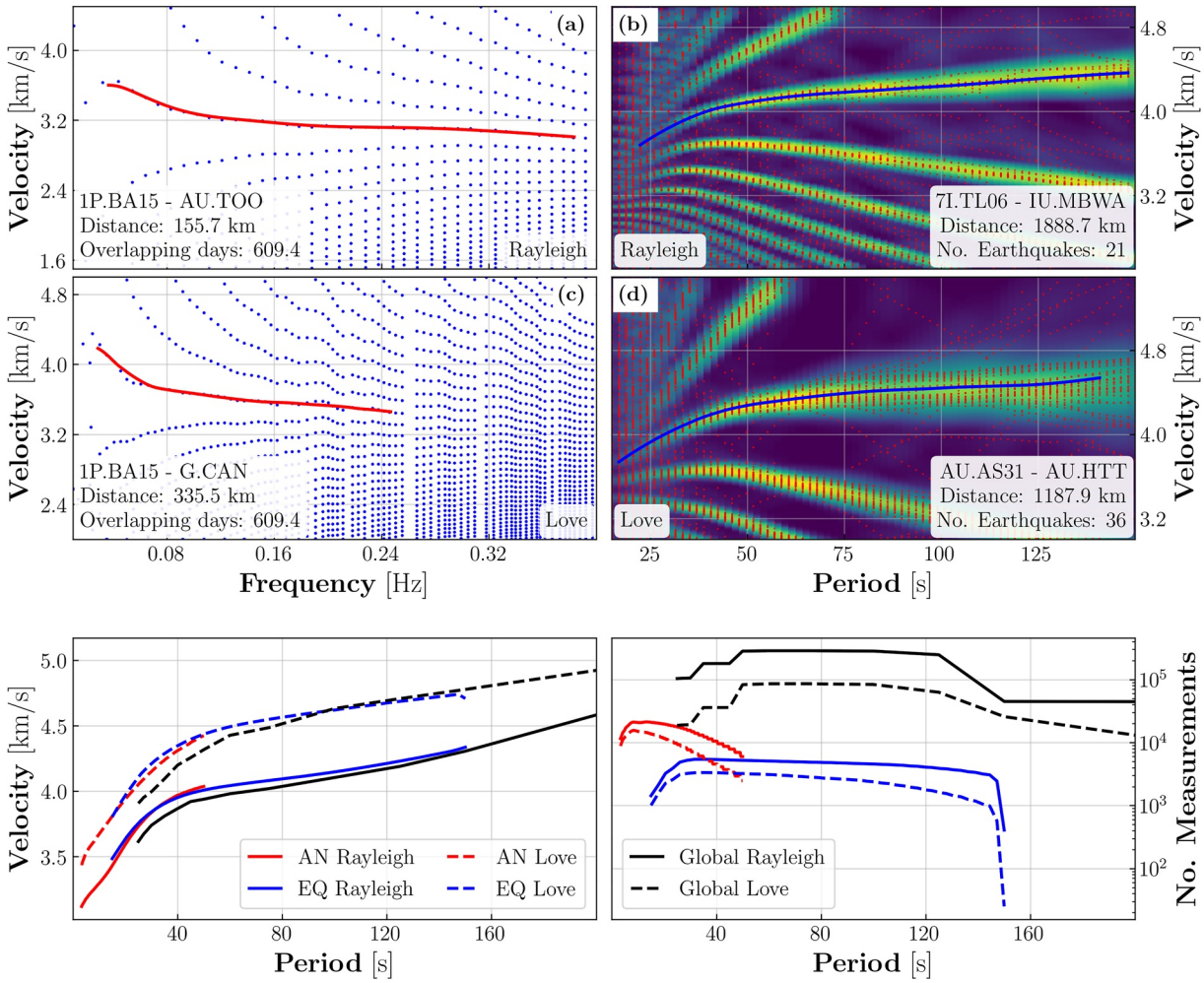

Figure 3. (a and c): zero crossings (blue dots) and dispersion curves (red lines) obtained from the cross-correlation of seismic ambient noise (AN). (b and d): ensemble of dispersion measurements (red dots) and associated curves (blue lines) retrieved from teleseismic earthquakes (EQ) through a two-station method; the density of observed dispersion is indicated by the background color. Each of these panels (a–d) refers to a different receiver pair, with (a and b) showing Rayleigh-wave phase velocities, (c and d) Love-wave phase velocities. The lower panels provide statistical information on our data set of phase velocities. The left-hand panel compares the average dispersion curves obtained in this study from AN and EQ with those measured by Ekström (2011) on a global scale. The corresponding number of measurements as a function of period is shown on the right.

aligned with at least 8 epicenters at a maximum distance of 3,000 km. (b) For each pair, we then collect dispersion measurements using all the aligned earthquakes individually. We do so by measuring ϕ (via cross-correlation) at different surface-wave periods and solving, at each period, Equation 1 for c. Specifically, we carry out this analysis at 75 discrete periods linearly spaced between 15 and 150 s, allow n to vary between ± 10, and consider values of c within the velocity range 2.5–5.5 km/s. (c) For a given station pair, we join all the (ambiguous) phase velocities obtained from the available earthquakes, to form an ensemble of dispersion measurements (Figures 3b and 3d). (d) From these data points, we produce a density map of the observed dispersion (background color in Figures 3b and 3d), which is finally used to pick the average inter-station dispersion curve (for technical details, see Magrini, Lauro, et al., 2022).

By applying the two-station algorithm described above, we retrieve 6,007 Rayleigh- and 3,900 Love-wave dispersion curves (Figure 3) spanning the period range 15–150 s. The number of earthquakes used to measure each dispersion curve is reported in Figure S1 in Supporting Information S1.

3.3. Global Measurements

We augment our new data set of Rayleigh and Love dispersion curves through phase-velocity measurements obtained at the global scale by Ekström (2011), covering the period range 25–200 s (Figure 3). Such measurements

were obtained from teleseismic earthquakes using a one-station method that is sensitive to velocity variations between a given epicenter-seismometer pair. Similar to previous studies (e.g., Kästle et al., 2018; Korostelev et al., 2022), only a limited portion of this global data set provides sensitivity to our study area, that is, continental Australia. Nonetheless, its use enhances the data coverage in regions characterized by relatively few inter-station paths, especially at long periods. Moreover, it gives us constraints at surface-wave periods longer than 150 s (i.e., the longest period reached by our dispersion curves), thus providing us with a robust background model in the inversion for shear-wave velocities (Section 5).

4. Spatial Variations in Surface-Wave Velocity

We translate our data set of Rayleigh and Love phase velocities into spatial velocity variations at different periods using SeisLib, which implements a linearized least-squares inversion scheme based on ray theory (e.g., Boschi & Dziewonski, 1999; Ekström, 2014) and the use of adaptive parameterization (Magrini, Lauro, et al., 2022).

4.1. Forward Problem

The method we use rests on the assumption that surface waves travel between two points on the Earth's surface along the great-circle path connecting them. In discrete form, the *forward* equation for the traveltime between these two points is $t = \sum_n s_n l_n$, where s denotes the slowness (in s/m) associated with each block n of the parameterized Earth's surface, and l the portion of the great circle (in m) crossing n.

At a given surface-wave period, our observables (i.e., inter-station phase-velocity measurements) are more conveniently expressed in terms of observed slowness, rather than traveltime; this is simply achieved by dividing both sides of the above forward equation by the total length L of the corresponding great-circle path. If we now define the $m \times n$ matrix such that $A_{ij} = l_j/L_i$, where the subscripts i and j denote the ith observation and jth block of the parameterization, respectively, we can switch to matrix notation and write

$$\mathbf{A} \cdot \mathbf{x} = \mathbf{b}, \tag{2}$$

where $\mathbf{b}$ denotes the m-vector whose ith entry is the reciprocal of the ith phase-velocity measurement, and $\mathbf{x}$ the n-vector whose jth entry corresponds to the slowness of the jth block (i.e., the unknown in the inversion).

4.2. Inverse Problem

In geophysical applications, the system of linear Equation 2 is usually ill-conditioned, meaning that it is not possible to find an exact solution for $\mathbf{x}$ (e.g., Rawlinson & Sambridge, 2003; Rawlinson et al., 2010) (In our case, it is strongly overdetermined at all periods, i.e., $m \gg n$.) Similar to previous surface-wave studies (e.g., Boschi & Dziewonski, 1999; Ekström, 2014), we overcome this issue by first assuming that the target slowness model is approximately known, that is, $\mathbf{x}_0 \sim \mathbf{x}$. We then invert for the regularized least-squares solution

$$\mathbf{x} = \mathbf{x}_0 + \left(\mathbf{A}^T \cdot \mathbf{A} + \mu^2 \mathbf{R}^T \cdot \mathbf{R}\right)^{-1} \cdot \mathbf{A}^T \cdot (\mathrm{b} - \mathrm{A} \cdot \mathbf{x}_0) \tag{3}$$

(Aster et al., 2018), where the roughness of the final model is determined by the scalar weight μ (that we choose via L-curve analysis, Hansen, 1999) and the roughness operator $\mathbf{R}$ depends on the parameterization (for technical details on its computation, see Magrini, Lauro, et al., 2022).

In practice, we use the average inter-station slowness observed in our data set at each period as a constant reference model $\mathbf{x}_0$, and solve Equation 3 via Cholesky factorization (e.g., Trefethen & Bau, 1997) of the matrix $\mathbf{A}^T \cdot \mathbf{A}$.

4.3. Parameterization

We parameterize the study area through an *adaptive parameterization*, allowing for higher resolution in the areas with greater data coverage (Magrini, Lauro, et al., 2022). Our strategy, illustrated in Figure 4 (see also Figure S2 in Supporting Information S1), follows a five-step procedure. (a) We initially define a global, equal-area parameterization consisting of relatively large blocks, each of $6.4° \times 6.4°$ (Figure 4a). (b) We then consider a relatively

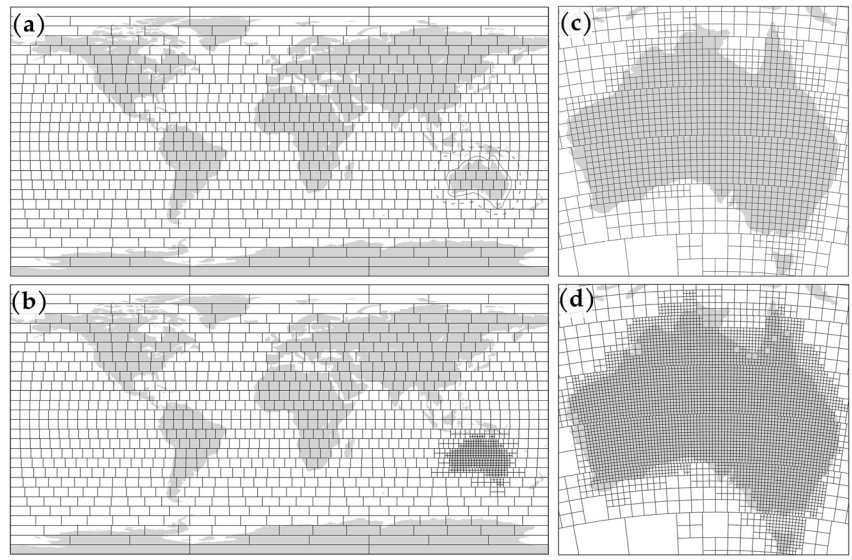

Figure 4. Illustration of our adaptive-parameterization strategy (Section 4.3), based on Rayleigh-wave phase velocity measurements at 30 s period. Note the two polygons (dashed and continuous red lines) in panel (a), employed to enhance resolution across Australia while limiting the total number of blocks defined at the global scale. The final, adaptive parameterization, shown in panel (d), displays blocks of five different sizes, that is, 0.4° (across most of Australia), 0.8° (across Australia and its close surroundings), 1.6° and 3.2° (in the region between the two aforementioned polygons), and 6.4° (throughout the rest of the world).

large polygon enclosing Australia and its surroundings (dashed red line in Figure 4a), and refine the parameterization by splitting all blocks inside it into four equal-area sub-blocks of 3.2° × 3.2° (Figure 4b). (c) We repeat step (b), this time based on a smaller polygon drawn around Australia and its immediate shelf region (continuous red line in Figure 4a); as a result, all blocks tessellating Australia have a size of 1.6° × 1.6° (Figure 4b).

The above three steps are *independent* of the number of measurements available at a given period. That is to say, we could have achieved an equivalent resolution across Australia by defining an equal-area parameterization of 1.6° × 1.6° at the global scale directly; this, however, would have resulted in a much larger number of parameters, and hence a computationally more expensive solution of our seismic inverse problems (for a discussion on the benefits of adaptive parameterizations, see Magrini, Lauro, et al., 2022).

The last two steps of our strategy are, instead, *dependent* on the available measurements. (d) We first calculate the number of inter-station (or epicenter-station) great-circle paths passing through each parameterization block obtained thus far. We then refine all those falling within the larger polygon described above, with the additional condition that they are intersected by more than 400 rays (Figure 4c) (We set this threshold to 25 rays at periods <25 s, i.e., at all periods that are not covered by the global data set discussed in Section 3.3.) (e) Finally, we repeat step (d), this time considering all blocks falling within the aforementioned smaller polygon and using a threshold of 200 rays (15 rays in the absence of global measurements). As shown in Figure 4d, the resulting parameterization is characterized by a maximum resolution of 0.4°; this is found in the areas intersected by a relatively large number of rays, which includes most of Australia.

4.4. Phase-Velocity Maps

We apply the above inversion scheme to calculate Rayleigh and Love phase-velocity maps at 21 discrete periods in the range 4–200 s. Visual inspection of our maps, several of which shown in Figure 5, suggests that the retrieved spatial variations in phase velocity reflect known geologic features of Australia.

At relatively short periods (maps at 5, 10, 15, and 20 s in Figure 5), most sensitive to the crust, we find evidence of the Archean basement in western Australia, with the Yilgarn and Pilbara cratons characterized by higher-than-average phase velocities. By contrast, low velocities correlate well with the thicker sedimentary layers found across the continent (compare Figures 1 and 5). At longer periods (75 and 125 s in Figure 5),

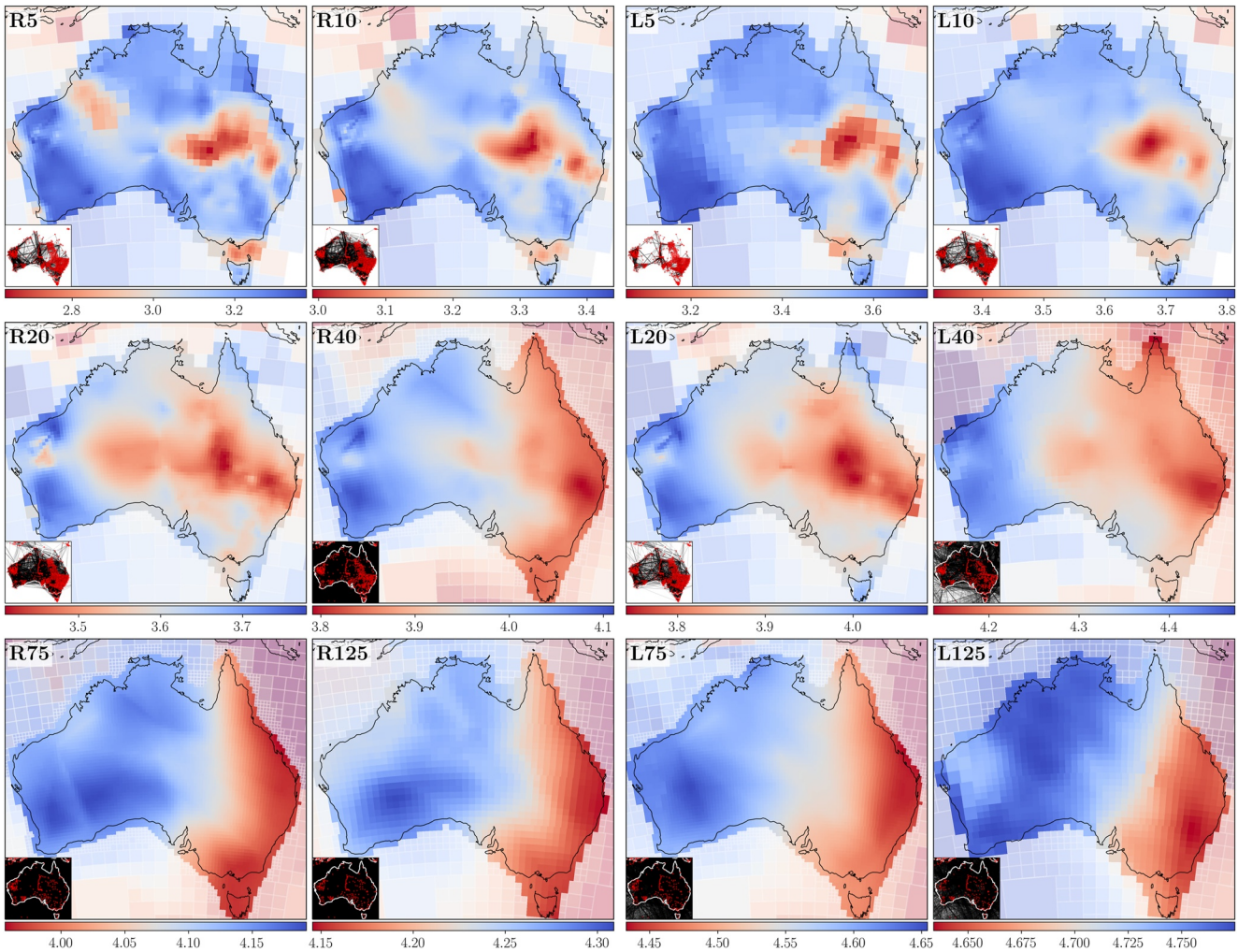

Figure 5. Rayleigh (R) and Love (L) phase-velocity maps (in km/s) at the periods of 5, 10, 20, 40, 75, and 125 s. A sub-plot in the lower left of each map indicates the raypath coverage, that is, the receiver pairs for which inter-station phase velocities were available at the corresponding period; these are represented by red dots and black lines drawn along the great circle connecting them. The masked areas, outside continental Australia, are not discussed in this study.

sensitive to upper-mantle depths, the most prominent feature of our maps is a large-scale eastward velocity decrease, previously attributed to higher temperatures found in the east in comparison to the older and colder cratonic part of Australia (Kennett et al., 2013, 2018).

4.4.1. Reconstruction Tests

To further substantiate the robustness of our phase-velocity maps, we carry out reconstruction tests at different periods. In practice, we first choose a reference velocity to define a constant velocity model at the global scale (The absolute value of such a reference—here, the average inter-station phase velocity at the target period—has no impact on the result of the tests.) We then perturb this model across Australia, to produce a checkerboard pattern of velocity anomalies in the range ± 10% with respect to the reference. Similar to Section 4.3, we parameterize the synthetic model through coarse blocks (8° × 8°) at the global scale, and fine blocks (up to a maximum resolution of 0.5°) across Australia; as shown in Figure 6, this results in smooth variations of the checkerboard patterns throughout the continent.

From the above velocity model, we define a synthetic model of slowness $\mathbf{x}_s$, and compute the data-kernel $\mathbf{A}_s$ associated with the chosen (synthetic) parameterization. We then calculate synthetic observations of inter-station (or epicenter-station) slowness $\mathbf{b}_s = \mathbf{A}_s \cdot \mathbf{x}_s$. Finally, we invert the synthetic data to determine the damped least-squares solution Equation 3, using the same parameterization and roughness damping μ employed in the calculation of our phase-velocity maps.

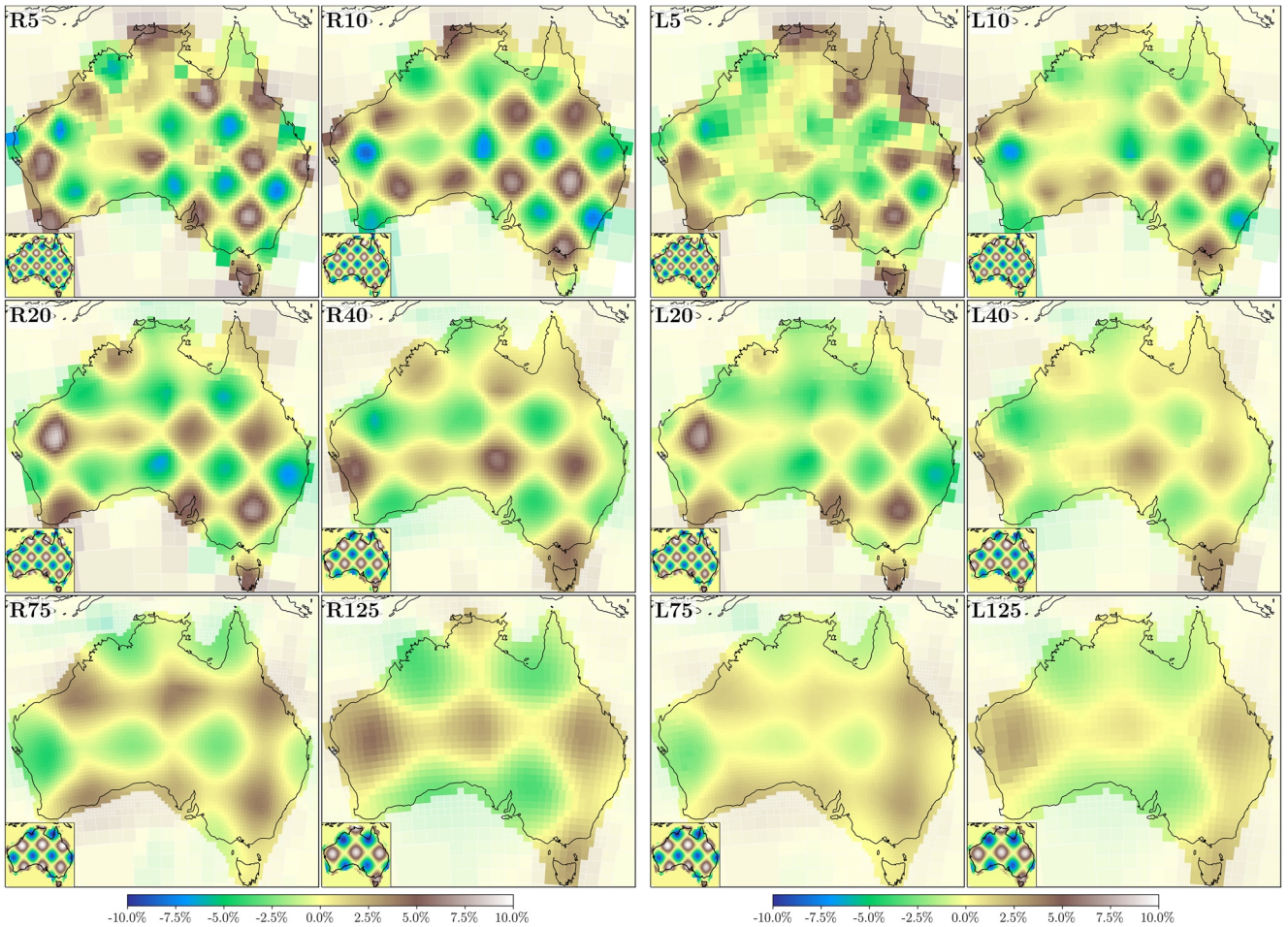

Figure 6. Reconstruction tests at the same surface-wave periods shown in Figure 5. At each period, the synthetic checkerboard pattern of velocity variations (i.e., the input model) is reported on the lower left. The color palette, constant across all maps, is expressed in percent with respect to the reference velocity used to produce the input model (Section 4.4.1).

The results of these tests, shown in Figure 6, point to the robustness of our maps. In general, the synthetic models are better retrieved from our Rayleigh-wave data set, due to the larger number of measurements available, although the Love-wave results are satisfactory. The recovered checkerboard patterns faithfully reproduce the synthetic inputs, with the shorter and longer periods constraining relatively short spatial variations and macro-scale features across the continent, respectively.

5. Inversion for Shear-Wave Velocity

We invert the Rayleigh and Love phase-velocity maps from Section 4 for depth variations in shear-wave velocity (V_S). Similar to previous studies (e.g., Magrini, Diaferia, et al., 2022; Saygin & Kennett, 2012), we first define an equal-area parameterization consisting of 4,586 blocks of 0.4° × 0.4°, covering continental Australia, and interpolate our phase-velocity maps onto it at each available period (Note that 0.4° is precisely the minimum grid spacing found across the adaptive maps discussed in Section 4.3; hence such an interpolation does not result in a loss of resolution.) We then use the interpolated maps to extract two phase-velocity profiles (one for Rayleigh and one for Love) for each location of the newly defined parameterization, spanning the period range 4–200 s. Under the assumption that vertically and horizontally polarized shear waves travel at the same speed ($V_{SV} = V_{SH}$), we finally invert each pair of phase-velocity profiles for isotropic V_S as a function of depth, and merge the results to obtain a 3-D shear-velocity model.

Over the last few decades, several strategies have been tested to invert Rayleigh and Love phase velocities for shear-wave velocity, with the main issue being a robust investigation of the parameter space (e.g., Lomax &

Snieder, 1994; Sambridge, 1999; Sambridge & Mosegaard, 2002; Wathelet, 2008). Here, we use a transdimensional Bayesian inversion scheme driven by a reversible-jump Markov chain Monte Carlo sampling (Bodin et al., 2012; Bodin & Sambridge, 2009), which can arguably be considered the state-of-the-art approach in geophysical inverse problems of this kind. The algorithm in this case belongs to an open-source Python package (BayHunter, Dreiling & Tilmann, 2019); its theoretical and algorithmic foundations, together with the main assumptions made in this study, are briefly summarized below.

5.1. Transdimensional Hierarchical Bayes

Consider the problem of finding the 1-D stratified Earth model $\mathbf{m}$ associated with a measurement of frequency-dependent phase velocity $\mathbf{d}$. Let us assume $\mathbf{m}$ is accurately approximated by a finite number of layers overlying a homogeneous half-space, each defined by its own thickness and physical properties such as V_S, compressional velocity V_P, and density ρ. The inverse problem inherent to finding $\mathbf{m}$ based on $\mathbf{d}$ is known to be nonlinear and *non-unique* (e.g., Foti et al., 2009), meaning that distinct predictions $\mathbf{d}_{pred} = g(\mathbf{m})$ will in general fit equally well the observations (here, the forward operator g is obtained using the Thomson-Haskell matrix method, Haskell, 1953; Thomson, 1950). In a Bayesian approach, this issue is tackled by representing all information (i.e., data fits and *a-priori* constraints) in probabilistic terms and by identifying, rather than a single well-fitting model, an *ensemble* of models that likely explain the observations. More specifically, Bayesian inference aims to quantify the *posterior probability* density function $p(\mathbf{m}|\mathbf{d}) \propto p(\mathbf{d}|\mathbf{m})p(\mathbf{m})$, where $p(x|y)$ denotes the probability of x given y and $p(\mathbf{m})$ the a-priori probability of $\mathbf{m}$.

Similar to Bodin et al. (2012), BayHunter samples the posterior iteratively, through a reversible-jump Markov chain Monte Carlo method. The inversion is initialized by randomly defining a 1-D model of the Earth. At each iteration, a new model is proposed via random perturbation of the "current" (i.e., the last accepted) model. Here, we allow for four different kinds of random perturbations: (a) a change in the thickness of a layer in the current model; (b) a change in the seismic properties of a layer; (c) the addition (or *birth*) of a new layer; (d) the removal (or *death*) of a layer. The latter two points make the inversion *transdimensional*, that is, the number of layers parameterizing the subsurface is an unknown itself, to be inferred from the data (e.g., Sambridge et al., 2006).

Each of the above random perturbations produces a new model from the last accepted one. The proposed model $\mathbf{m}'$ is then accepted with a probability proportional to the *likelihood*

$$p(\mathbf{d}|\mathbf{m}') = \frac{1}{2\pi\sigma_L\sigma_R}\exp\left(-\frac{(g_L(\mathbf{m}')-\mathbf{d}_L)^2}{2\sigma_L^2} - \frac{(g_R(\mathbf{m}')-\mathbf{d}_R)^2}{2\sigma_R^2}\right), \quad (4)$$

where the subscripts R and L denote Rayleigh and Love and σ the standard deviation of the data. Equation 4 implicitly assumes that the standard deviation of a dispersion curve is independent of period, and no correlation exists between different periods.

As shown in Bodin et al. (2012), the acceptance probability also depends on the standard deviation of the Gaussians used to perturb the physical (seismic) properties of each layer. In BayHunter, these are adjusted iteratively, so as to obtain optimal (Bodin et al., 2012) acceptance rates of 40%–45%. Moreover, the inversion algorithm employed in this study is *hierarchical*, meaning that the standard deviation of the data is treated as a free parameter. As a result, the arbitrary choice of a weighting factor for our Rayleigh and Love dispersion curves is avoided, since this aspect is driven by the data itself.

5.2. Technical Details

We parameterize each stratified, 1-D Earth model through 3 to 20 layers. We treat the V_S value of each layer and the bulk V_P/V_S ratio of the crust as unknowns (i.e., free variables), and set the maximum depth of the top of the homogeneous half-space to 300 km. We allow V_S and V_P/V_S to vary in the range 1.5–5.5 km/s and 1.4–2.1, respectively, according to uniform probability distributions. We fix the V_P/V_S ratio of the mantle to 1.8 (the value of a 1-D reference mantle, Dziewonski & Anderson, 1981) and link density to V_P through the empirical relationship $\rho = 0.32V_P + 0.77$ (Berteussen, 1977).

Note that Love waves have no sensitivity to V_P, and Rayleigh waves are only weakly sensitive to it (e.g., Wathelet, 2005). Specifically, Rayleigh-wave sensitivity to V_P is characterized by a peak at the surface, and

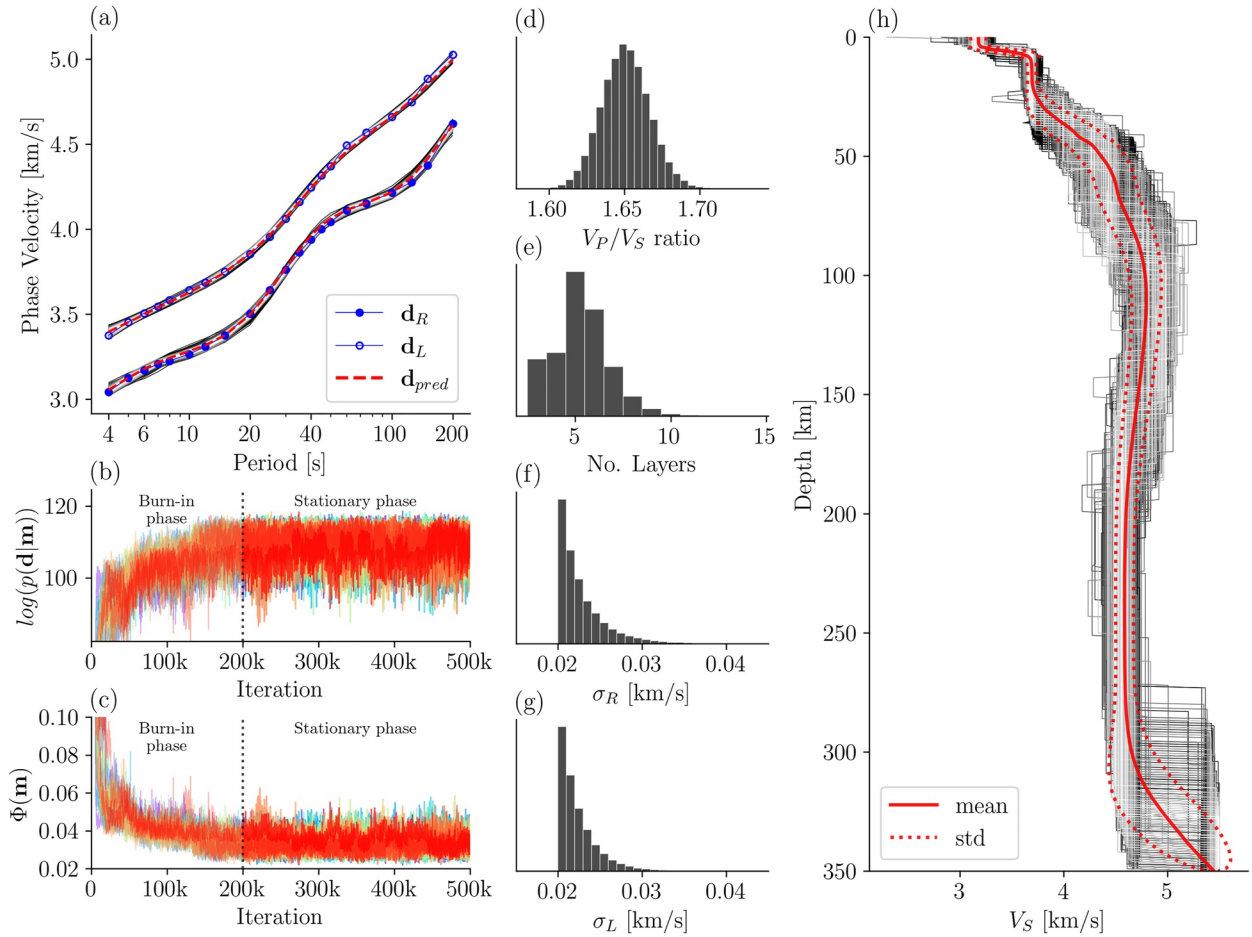

Figure 7. Illustration of the Bayesian inversion carried out in this study to obtain 1-D shear-wave-velocity models from Rayleigh ($\mathbf{d}_R$) and Love ($\mathbf{d}_L$) dispersion curves. (a): Observed (blue) and average predicted (red) dispersion curves. (b) and (c): Log-likelihood and average misfit $\Phi(\mathbf{m}) = \sqrt{\frac{(g_L(\mathbf{m}')-\mathbf{d}_L)^2+(g_R(\mathbf{m}')-\mathbf{d}_R)^2}{2}}$ as a function of iteration. The different colors refer to the 25 Markov chains employed in the inversion. (d) through (g): normalized histograms of crustal V_P/V_S, number of layers, and standard deviation of the data (σ_R and σ_L) associated with the ensemble of 150,000 models saved during the inversion. (h) Shear-velocity as a function of depth associated with the 150,000 models; each 1-D profile is color-coded in a gray scale according to the associated misfit (with white corresponding to lower misfits). The dispersion curves are computed based on these models, and used to calculate the average predicted dispersion curves as reported in panel (a) using the same color palette. The results illustrated in this figure refer to the geographic location 25.978°S 132.474°E.

decreases exponentially with increasing depths (Figure S3 in Supporting Information S1). In our case, therefore, the use of the V_P/V_S ratio as a free parameter is preferable to treating V_P as an unknown directly, since realistic values of crustal V_P/V_S fall inside a much tighter range than that spanned by V_P; such a tighter range translates into a smaller parameter space, and hence, in principle, into quicker convergence rates. The weak sensitivity of our data set to V_P also motivates the fixed V_P/V_S ratio for the mantle mentioned above.

We bound the standard deviation of the data within the range 0.02–0.1 km/s. For each pair of Rayleigh and Love phase-velocity profiles, we sample the posterior probability through 25 Markov chains, which we run in parallel for 500,000 iterations. We assume that the random walk is stationary starting from the 200,000th iteration of each chain (e.g., Bodin et al., 2012) and save one model every 50 iterations. This is illustrated in Figure 7.

Overall, the above procedure yields 150,000 models per location, which we ensemble average and spatially merge to obtain a 3-D shear-velocity model. We assess the vertical resolution of our model through synthetic tests, whose results are reported in Figures S5 and S6 in Supporting Information S1. These tests suggest that our data and inversion scheme are able to resolve the subsurface structure at high resolution up to at least 150 km depth. At greater depths, our shear-wave velocity model is characterized by relatively high uncertainty in its absolute value, due to the reduced sensitivity of fundamental-mode surface waves to V_S (see also Section 6.4). Arguably, the uncertainty on the retrieved spatial patterns is considerably smaller, as evidenced by the capability of our

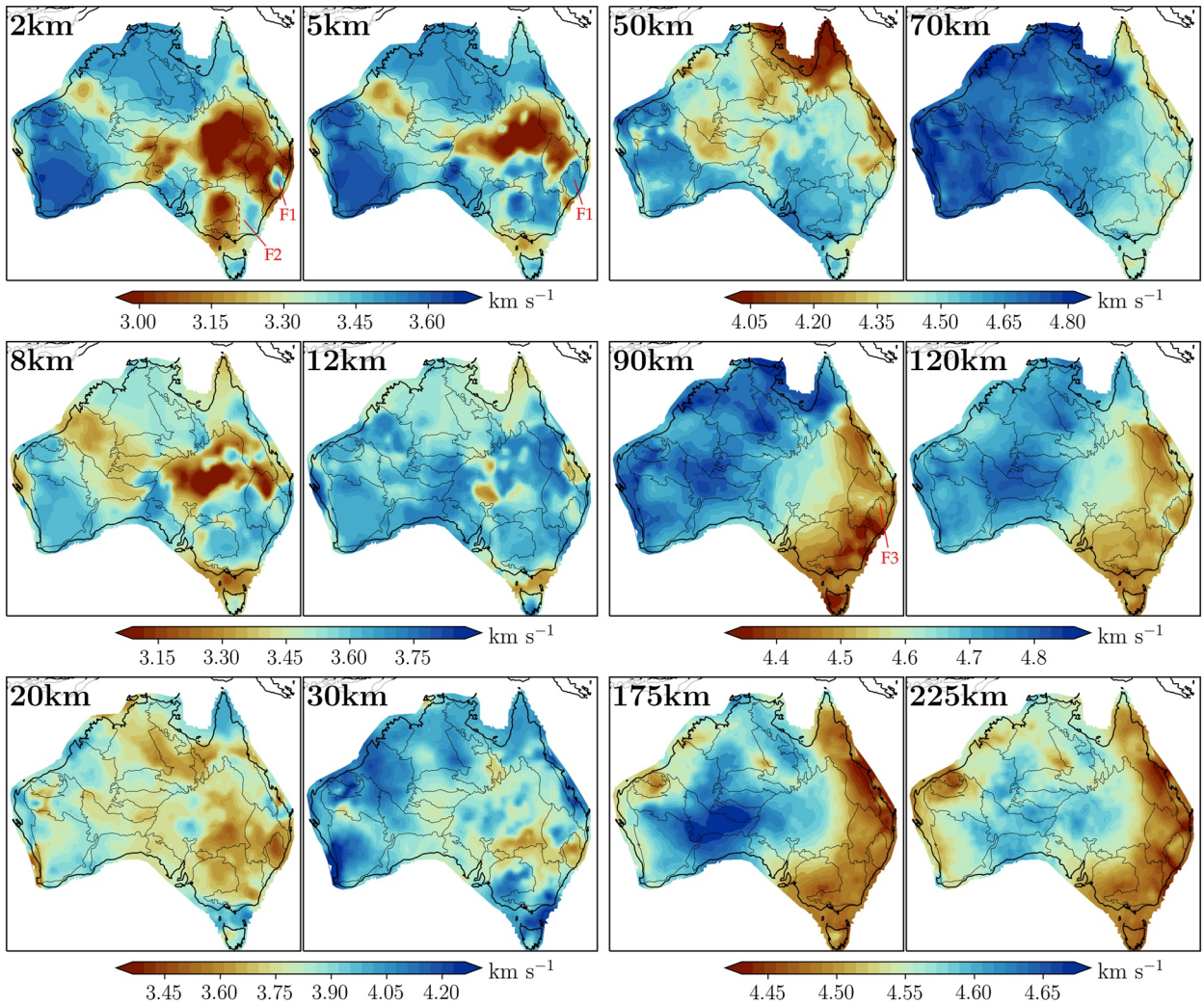

Figure 8. Maps of shear-wave velocity (in km/s) at different depths.

inversion scheme to resolve relatively small (±5%) variations in V_S below 150 km depth (Figure S6 in Supporting Information S1).

6. Discussion

Our shear-velocity model extends to 300 km depth, thus spanning both the crust and upper mantle of continental Australia. This is illustrated through horizontal slices and cross-sections in Figures 8–10. Because of the very large spatial extent of our tomographic model, we find it convenient to subdivide the following discussion into three parts. In the first two parts, we deal with its crustal (Section 6.1) and mantle (Section 6.2) features, while Section 6.3 focuses on a broad scale comparison of our model with AuSREM.

6.1. Crustal Structure

6.1.1. Sedimentary Basins

In the upper crust, our shear-wave velocity model displays relatively low velocities that nicely correlate with the extent of the sedimentary basins reported in the OZ SEEBASE® 2021 model (compare Figure 1b with the horizontal slices in Figure 8). In Western Australia, for example, one large-scale low-velocity region extends from the northwestern coastline to the center of the continent at up to 8 km depth, consistent with the location of the Canning and Amadeus basins. Phanerozoic eastern Australia appears to be broadly dominated by low-velocity

areas in the upper 2–12 km; this is outlined by the iso-velocity line at ∼3.15 km/s (see Figure 8), which could be considered, in our case, as a rough proxy for the thickness of sedimentary basins. In southeastern Australia, we find pronounced low velocities that correspond to the location of the Murray-Darling Basin, which are no longer visible at 5 km depth. Indeed, although most of the Murray-Darling Basin is relatively thin (of the order of a few hundreds of meters thick), it contains older pre-Tertiary infrabasins that are thicker (Li et al., 2021). Further north, the location of the wide Eromanga Basin is revealed by similarly low velocities, with some depocenters reaching depths greater than 8 km. Our results are also consistent with the targeted ambient noise imaging study of Pilia, Rawlinson, Direen, et al. (2015), which reveals low velocities in the upper crust consistent with the presence of failed rift basins. The relatively thick Mesozoic and Cenozoic sedimentary layers that mask the older basement make it challenging to unravel the tectonic assemblage of the Tasmanides.

In some cases, the geometries outlined by such low-velocity regions follow strikingly well known geological boundaries. This is especially visible across the eastern Australian coastline, whose structure is constrained by a large volume of data due to the very dense distribution of receivers available (Figure 2). Here, the Paleozoic New England and Lachlan orogens exhibit high velocities that are interrupted by the low velocities of the Sydney basin (slices at 2 and 5 km depth in Figure 8).

6.1.2. Cratons

A distinct change in shear-wave velocity from the regions covered by relatively recent sediments to those characterized by old outcropping rocks (Proterozoic and Archean) can be observed in our model. In the West Australian Craton, very high velocities (∼3.6 km/s, values that are typical of mid-to-lower crustal levels) characterize the Yilgarn and the Pilbara Craton, while lower velocities outline the domain of the Pinjarra Orogen. The separation between Pinjarra and the rest of the craton is clearly visible down to 8 km depth (Figure 8). At greater depths, the West Australian Craton features overall high velocities; these can be followed through the entire crust and upper mantle, indicating a thickened and cold lithospheric root underlying the area.

We find similar high velocities beneath the Gawler Craton (South Australian Craton) and, to some extent, the Kimberly Block (North Australian Craton). Up to 8 km depth, the velocities found in the Mt. Isa Province are, in their absolute value, very similar to those of the Gawler Craton, supporting the idea that they were both part of a greater proto-Australian continent (Betts & Giles, 2006; Giles et al., 2004). Our V_S model does not suggest that this is the case for the Arunta Province, albeit this could be ascribed to poorer resolution in the region (Figure 6). In the Gawler craton, we observe a velocity decrease with depth in the mid-lower crust (20–30 km). Although this feature may represent an actual change in the cratonic structure, it is more easily explained by the relatively small size of the craton itself compared to the resolution of the model (We remind the reader that our model is entirely derived from surface-wave velocity measurements, and that its deeper part is constrained by the longer periods, associated with longer wavelengths).

6.1.3. Tasmanides

To the east of the (probable) Neoproterozoic location of Rodinia breakup (Direen & Crawford, 2003a), Australia features the Phanerozoic accretionary system of the Tasmanides (e.g., Rosenbaum, 2018). As pointed out in Section 6.1.1, most of eastern Australia is dominated by low-velocity sedimentary cover that largely conceals the tectonic structure of this region. Nevertheless, we find two high-velocity areas that appear prominent at shallow depths. The first, visible in the horizontal slice at 2 km depth (Figure 8, feature F1), appears north-south trending and adjacent to the Boothera-Gandra fault (located to the east of the Murray Basin); as observed in Pilia, Rawlinson, Cayley, et al. (2015), this high-velocity feature reveals a strong correlation with the high-temperature metamorphic belts, Ordovician volcanic arcs, and granites of the Wagga-Omeo Metamorphic Complex. The second high-velocity feature (F2 in Figure 8) consists of a localized area, visible in the horizontal slices at 2 and 5 km depth, that highlights the New England Orogen. Although the New England Orogen has been previously associated with a relatively high magnetic intensity and low Bouguer gravity anomaly (Kennett et al., 2018), its seismic signature has not been shown with such clarity in previous studies.

6.1.4. Moho Proxy

We approximate the Moho depth with the 4.2 km/s iso-velocity contour (e.g., Dziewonski & Anderson, 1981). The depth variations of our Moho proxy, shown in Figure 11a, range from ∼30 km (western Australia and most of the Tasmanides) to ∼65 km (northernmost part of Queensland). The larger-scale features of our Moho map are in agreement with those inferred by Salmon et al. (2013) and Kennett et al. (2018, 2023), whose results are

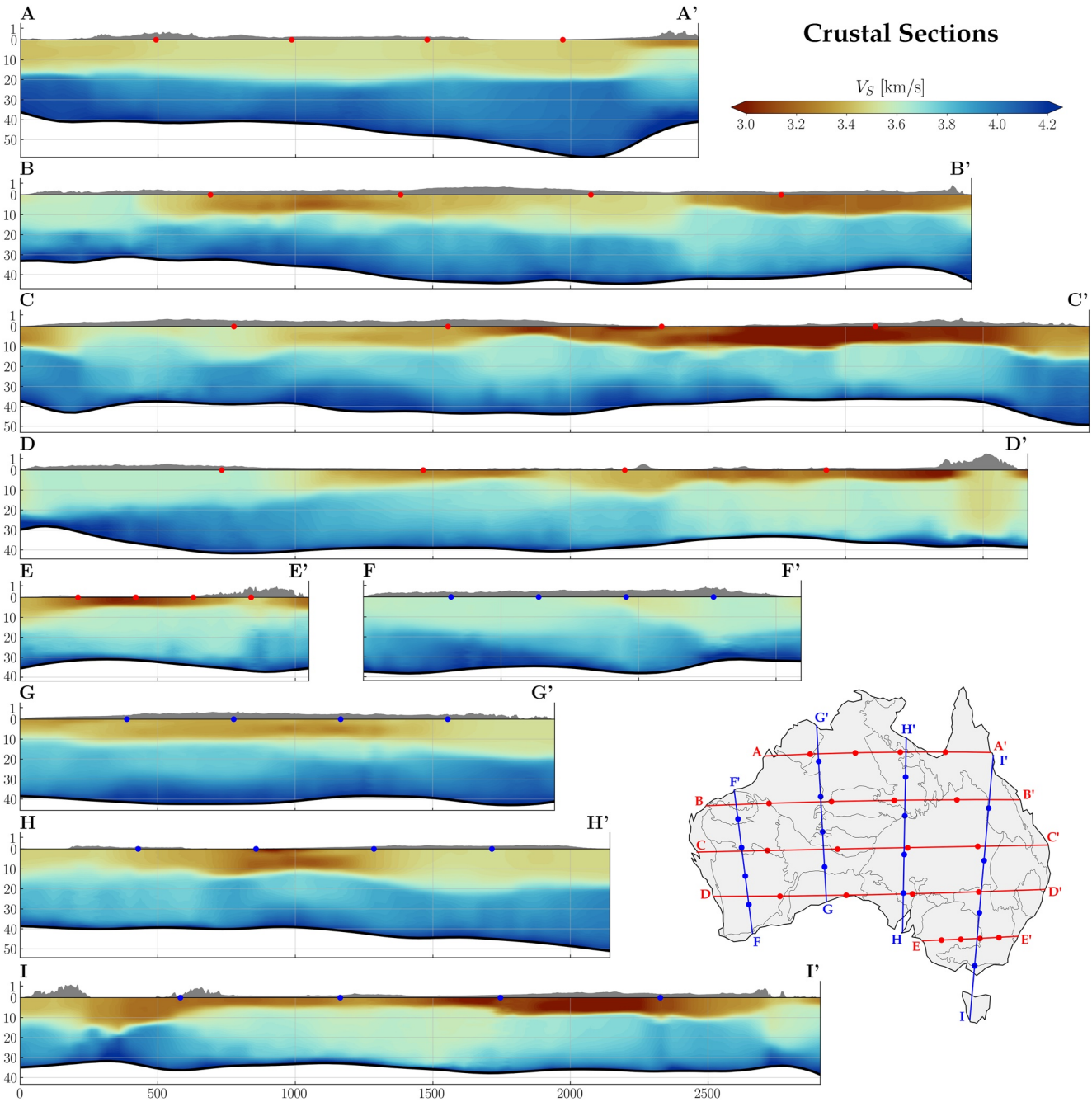

Figure 9. Crustal shear-velocity cross sections (distance vs. depth, both in km), with topography (gray) shown on top of each profile. Ticks on the *x*-axes are equally spaced across all sections by 500 km. The bold black line at the bottom of each cross-section corresponds to the Moho proxy, reported in Figure 11.

based on receiver functions, reflection, and refraction data. Similar to these studies, we observe relatively shallow Moho depths (~32 km) beneath the Yilgarn and the Pilbara Craton and a slightly thicker crust (~40 km) between them, corresponding to the location of the Capricorn Orogen. A relatively deep Moho (~40–45 km) spans Central Australia, largely covered by Cenozoic Terranes, and both the Kimberly and Gawler Cratons. To the east, across the Tasmanides, crustal thickness once again decreases to ~32–36 km, with a minimum approximately centered on the Murray Basin.

The most significant discrepancy between the Moho depth reported in Kennett et al. (2023) (Figure 11c) and our proxy is found across the northernmost part of Queensland. Here, our proxy points to very large Moho depths of ~60–65 km, while no significant anomaly is observed in Kennett et al. (2023). Such a large

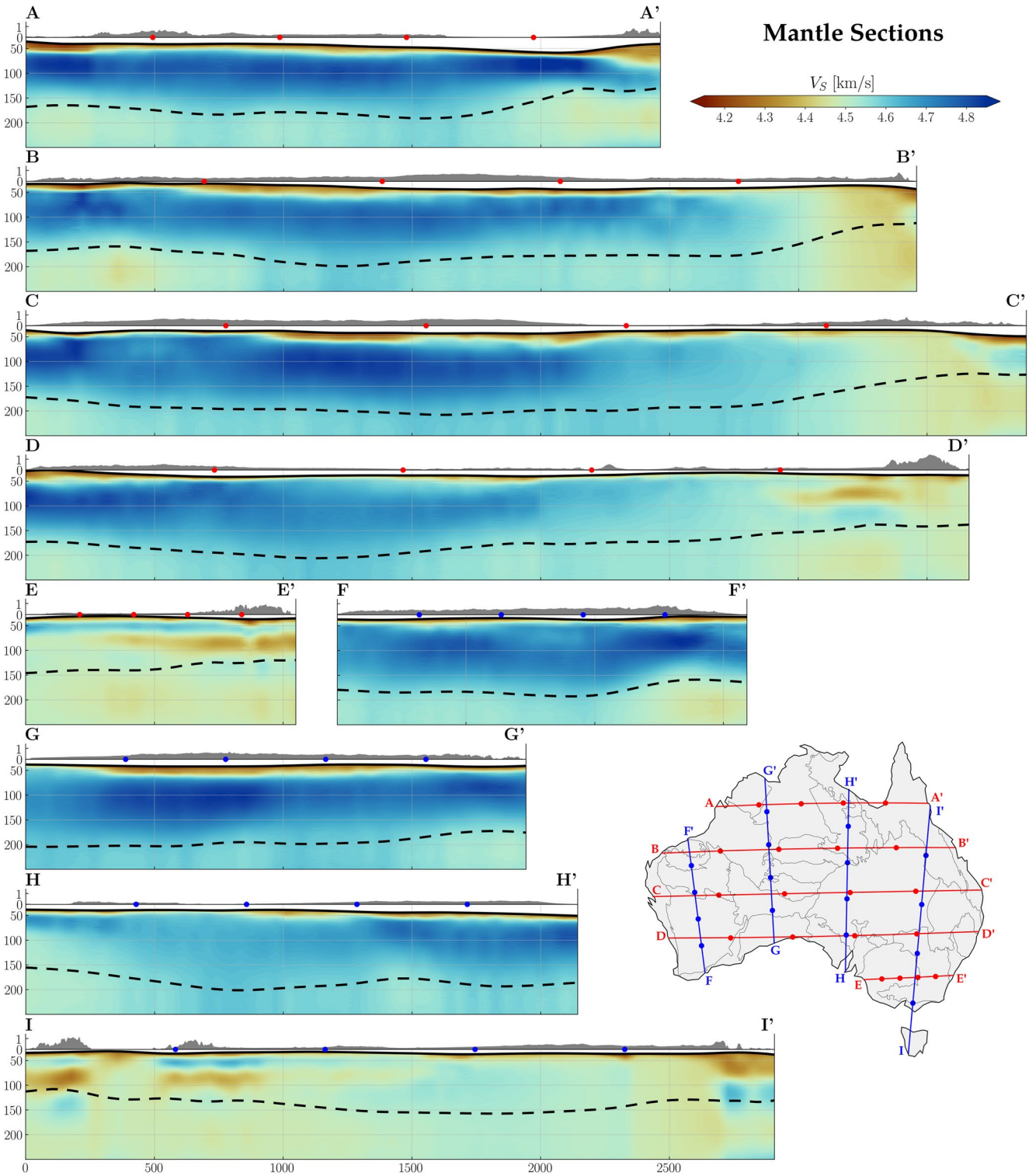

Figure 10. Similar to Figure 9, but now extending to upper-mantle depths. Within each cross-section, the dashed black line denotes the LAB proxy, whose spatial variations are shown in Figure 11.

Moho-depth anomaly most probably represents an artifact in our model. In fact, the region in question is characterized by a sparsity of receivers (Figure 2), resulting in sub-optimal spatial resolutions of our phase-velocity maps, especially at shorter periods (Figure 6). In addition, the uncertainty in our Moho proxy is arguably very

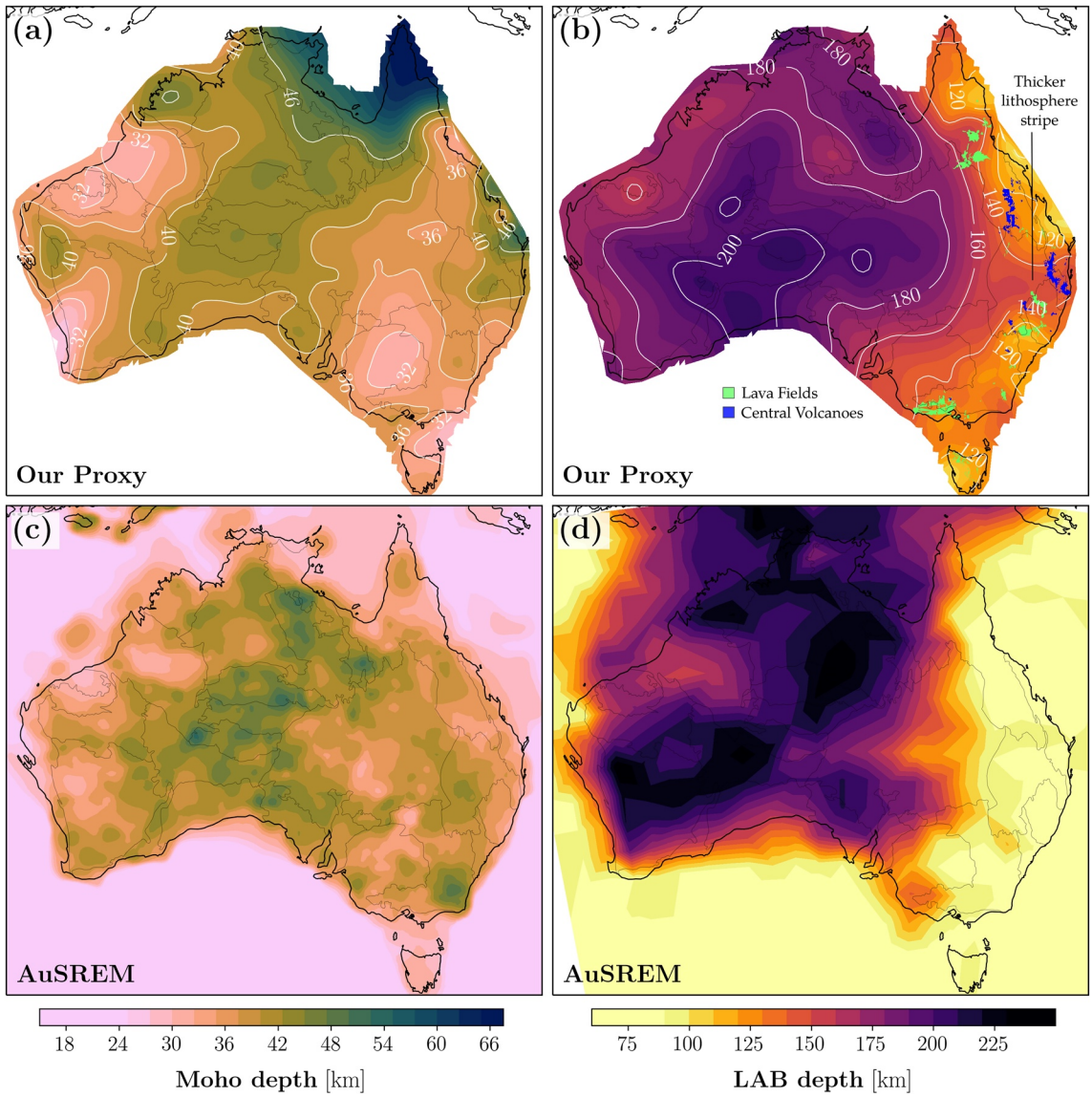

Figure 11. Depth maps of Moho (left) and LAB (right). Panels (a and b) correspond to the proxies inferred from our 3-D shear-velocity model (Sections 6.1.4 and 6.2.1). Panels (c and d) show the Moho and LAB depths as reported in AuSREM (Kennett et al., 2018, 2023). Eastern Australian Cenozoic intraplate volcanism, shown in panel (b) in the form of blue and green polygons, was drawn after Rawlinson et al. (2017).

large in this region: our 1-D depth profiles show a thick layer at ~20–40 km depth characterized by shear velocities of ~4.1 km/s (Figure 8, slices at 30 and 50 km). It is thus difficult to attribute this layer to either crustal or mantle material, an intrinsic limitation when defining the depth interfaces from the inversion of surface waves alone.

We find a similar depth uncertainty under the New England Fold Belt, where the 4.2 km/s iso-velocity contour results in crustal thicknesses of up to 46 km. In this case, however, the relatively large Moho estimates may be linked to actual geologic features, such as crustal thickening related to the formation of the New England Orogen or the presence of underplated material (e.g., Finlayson & Collins, 1993).

Obviously, different choices in the iso-velocity contour would result in different estimates of crustal thickness. The absolute value of a surface-wave-based proxy such as that presented here should therefore be treated with caution. The uncertainty on the lateral variations of our Moho-depth estimates is arguably much smaller. In fact, the large-scale spatial patterns of our proxy are mainly left unchanged by slightly different choices in the iso-velocity contour (Figure S7 in Supporting Information S1), which highlights their robustness.

6.2. Mantle Structure

The use of teleseismic data, associated with longer-period surface waves, allows for the investigation of the V_S structure up to relatively large depths, with the key advantage of providing a continuous model from the surface to the upper mantle. In our model, we find high-velocity zones just below the Moho in the west, beneath the Yilgarn and Pilbara cratons, as well as beneath the southern Tasmanides (see slice at 50 km depth in Figure 8). The Pn-wave study of Sun and Kennett (2016) shows similar lateral velocity variations, but includes shorter-wavelength structures. While our V_S model displays simpler patterns of velocity variations with increasing depth, Sun and Kennett (2016) point to pronounced small-scale anomalies below the Canning basin and in central Australia, approximately below the Amadeus Basin. In surface-wave studies, an increase in velocity uncertainty is generally associated with increasing period (corresponding to increasing depths), due to the lower spatial resolution (e.g., Kästle et al., 2018; Magrini, Diaferia, et al., 2022). This may lead, for instance, to a trade-off between the velocity structure right above and below the Moho. In our view, it is unclear whether the absence of the aforementioned small-scale anomalies in our model should be ascribed to the lower spatial resolution of surface waves or to differences in sensitivity to the physical properties of the mantle between surface waves and P- and S-waves (used by Sun and Kennett (2016)).

At greater depths (>70 km), the most prominent feature of our model is a large-scale decrease in shear-wave velocity from west to east (Figure 8). In its western and central part, the Australian upper mantle presents shear velocities of up to 4.9 km/s, which is almost 10% faster than a typical 1-D reference mantle (e.g., Dziewonski & Anderson, 1981). The remaining eastern part of Australia shows significantly lower velocities. This pattern can be followed from approximately 70 km depth to more than 120 km depth. At even larger depths, the absolute velocity differences between east and west become less prominent, albeit leaving the large-scale pattern of velocity decreasing eastward almost unchanged.

Such an east-west contrast in the seismic signature of the Australian mantle has been observed in previous tomographic studies (e.g., Fichtner et al., 2010; Fishwick et al., 2008; Yoshizawa & Kennett, 2004; Zielhuis & van der Hilst, 1996), which attributed the presence of the above velocity gradient to a transition from Precambrian to Phanerozoic terranes. Intriguingly, in the Tasmanides our V_S model also features a narrow corridor of higher-than-average velocities (with respect to those found in the same region) that propagates eastward beneath the New England Orogen (F3 in Figure 8, slice at 90 km). A similar feature, both in shape and absolute value, has been observed in a wide depth range using both full-waveform (Fichtner et al., 2010) and P-wave travel-time tomography (Rawlinson et al., 2014), and was hypothesized to have played an important role in creating the complex orocline bending of the New England Orogen.

6.2.1. LAB Proxy

Following Priestley and McKenzie (2006), we use our 3-D shear-wave velocity model to retrieve a proxy for lithosphere-asthenosphere boundary (LAB) depth. To do so, we first convert our V_S model into temperature by finding the solution, in least-squares sense, to the equation

$$V_S - [1 + b(z - 50000)]\left[m(T - 273) + c + A\exp\left(-\frac{E + PV_a}{RT}\right)\right] = 0, \quad (5)$$

where V_S and the sought temperature T (in K) are a function of location and depth (z, in m). $A = -1.8 \times 10^{16}$ m/s, $b = 3.84 \times 10^{-7}$ m^{-1}, $c = 4{,}720$ m/s, $E = 409 \times 10^3$ KJ/mol, $m = -2.8 \times 10^{-1}$ m/s, and $V_a = 10^{-6}$ m^3/mol are empirically fitted constants (Priestley & McKenzie, 2006). Pressure $P = \rho g z$ is assumed to be lithostatic, with gravity acceleration $g = 9.81$ m/s^2 and density $\rho = 3{,}300$ g/m^3. Expression 5 builds on constraints from oceanic lithosphere, but has been applied successfully to a broad range of tectonic settings (Greenfield et al., 2022; Priestley & McKenzie, 2006; Roberts et al., 2018).

We then estimate the LAB depth by taking the 1300°C iso-surface of the retrieved temperature model. The lateral variations of our LAB proxy are shown in Figure 11b, and indicate lithospheric thicknesses of ∼170–205 km in western and central Australia and of ∼120–160 km in the east. This result concurs with previous hypotheses (Davies et al., 2015; Rawlinson et al., 2017) for which Cainozoic intraplate volcanism in eastern Australia is largely controlled by lithospheric thickness. Indeed, a thicker lithosphere would prevent or partially suppress decompression melting, rendering the generation of volcanism at the surface unlikely.

Visual inspection of Figure 11b also suggests that the high-velocity corridor visible in eastern Australia at 90 km depth (feature F3 in Figure 8) translates into a region of thicker lithosphere in our LAB map, similar to Davies

et al. (2015) and Rawlinson et al. (2017). Such a stripe of thicker lithosphere, extending east to the coast, appears to be associated with a compositional change in the surface volcanism, as indicated by the distribution of central volcanoes and lava fields in Figure 11b. Incidentally, this observation supports the hypothesis, initially advanced by Davies et al. (2015), that variations in lithospheric thickness beneath eastern Australia can lead to a change in both composition and amount of volcanism at the surface.

Similar to Section 6.1.4, while different temperature iso-surface choices will necessarily lead to differences in the retrieved lithospheric thickness, the spatial patterns of our proxy are affected to a much smaller extent compared to its absolute values (Figure S8 in Supporting Information S1). This provides further confidence in the above interpretation.

6.3. Comparison With AuSREM

As noted previously, AuSREM combines different seismological information to create a geophysical synthesis of the Australian crust and mantle (Kennett et al., 2018). Such a synthesis involved the use of P- and S-wave velocity models independently derived from reflection and refraction data, receiver functions, ambient-noise and earthquake-based measurements (Kennett et al., 2013; Salmon et al., 2013; Sun & Kennett, 2016; Yoshizawa, 2014; Yoshizawa & Kennett, 2015).

With respect to the shear-wave component of AuSREM, the clearest improvement in our model concerns the crustal structure. At the continental scale, the main patterns of shear-velocity variations across the Australian crust, as reported in Saygin and Kennett (2012), are consistent with those discussed in Section 6.1. Relatively low velocities characterize the sedimentary basins, while higher-than-average velocities are found across the main cratonic blocks. The model of Saygin and Kennett (2012), however, relied on fewer receivers than in this study (compare Figure 2 with their Figure 1) and was derived from ambient-noise group-velocity measurements, which only allowed for constraining the upper 20–25 km of the crust (see also Salmon et al., 2013). The improved seismic coverage used here, together with the use of phase velocities in a broad period range (4–200 s), allowed us to retrieve shear-wave velocity variations down to upper-mantle depths and at significantly higher resolution (compare our Figures 8 and 9 with Figures 9 and 10 in Saygin and Kennett (2012)).

The joint inversion of Rayleigh and Love phase velocities measured from both seismic ambient noise and teleseismic earthquakes therefore allow us to cover an important gap in the S-wave component of AuSREM: a gap spanning lower-crustal to uppermost-mantle depths. In fact, most tomographic studies of the Australian crust and uppermost mantle have been carried out only at regional or local scale (e.g., Crowder et al., 2019; Pilia et al., 2013; Pilia, Rawlinson, Direen, et al., 2015; Young et al., 2013; Yuan & Bodin, 2018), thus making our model the first, in the depth range ~30–50 km, to illuminate the entire continent at high resolution. For the same reason, our study also provides, for the first time, continent-wide estimates of Moho depth without resorting to the interpolation of sparse, punctual measurements collected across the continent. Naturally, our surface-wave-based proxy (Figure 11) cannot be considered as a reliable Moho-depth model as those derived, at the smaller scale, from receiver functions and active seismic methods (see Kennett et al., 2023, and citations therein). In fact, compared to more ad hoc approaches, surface waves have poorer sensitivity to sharp discontinuities (e.g., Bodin et al., 2012; Lebedev et al., 2013; Molinari & Morelli, 2011). Nonetheless, the main features of our proxy resemble those of the interpolated map reported in AuSREM (see Section 6.1.4).

In the depth range 70–250 km, the shear-wave velocities retrieved in this study appear consistent with those reported in AuSREM, in both their absolute values and in their large-scale spatial patterns (compare Figures 8 and 10 with Figures 8.2 and 8 of Kennett et al., 2018). While, at these depths, our study arguably does not contribute significantly to the existing literature, this result provides additional confidence in the overall robustness of our V_S model.

A somewhat more interesting comparison involves the AuSREM's map of LAB depth and that obtained from our model (Figures 11b and 11d). In general, our estimates are more moderate compared to AuSREM, where lithospheric thickness is as large as 220 km in the west and reaches values as small as 80 km in the east (Figure 11d). We note, however, that the AuSREM's estimates build on measurements from refracted waves, surface- and body-wave tomography, and on the analysis of both absolute velocities and velocity gradients. Recent receiver-function studies have been unable to reproduce the same pattern of LAB depths, which indicates that the LAB may not be characterized by strong velocity gradients (Birkey et al., 2021; Ford et al., 2010). Instead, these studies have

interpreted several of the observed phase conversions as resulting from mid-lithospheric discontinuities (MLD) at 80–120 km depth, where we inferred depths of more than 150 km. The MLD have also been discussed in relation to vertical changes in radial anisotropy (Yoshizawa & Kennett, 2015) and multi-scale heterogeneities (Kennett et al., 2017; Sun et al., 2018). Joint inversions of receiver functions and surface waves can be helpful in reconciling these different types of data to investigate upper-mantle boundaries such as the LAB and Lehmann discontinuity (e.g., Bodin et al., 2012; Calò et al., 2016; Taira & Yoshizawa, 2020).

In terms of relative variations, the most relevant discrepancy between the LAB-depth maps in Figures 11b and 11d concerns the mentioned stripe of thicker lithosphere extending to the east coast; this is visible both in our proxy and in previous studies (Davies et al., 2015; Rawlinson et al., 2017), but absent in AuSREM.

6.4. Limitations of Our Model

Unlike previous tomographic studies of the Australian upper mantle that incorporated surface-wave higher modes (Debayle & Kennett, 2000a; Fishwick et al., 2008; Kennett et al., 2013; Yoshizawa & Kennett, 2004; Yoshizawa & Kennett, 2015; Zielhuis & van der Hilst, 1996), this work focused exclusively on fundamental modes. Inversions of multi-mode surface-wave velocities have been shown to benefit vertical resolution at relatively large upper-mantle depths (Yoshizawa, 2014), around which the cratonic LAB may exist. In fact, fundamental-mode Love waves exhibit poor sensitivity to variations in V_S below 200 km depth, even at the longest surface-wave periods available in our data set. Fundamental-mode Rayleigh waves are more sensitive to deep structures, but their sensitivity kernels at 150–200 s are broadened over a wide depth range (Figure S4 in Supporting Information S1). Consequently, at depths greater than 200 km, the V_S structure retrieved from the inversion of fundamental modes can be affected by vertical smearing (Figure S6 in Supporting Information S1; see also Yoshizawa, 2014). This potential issue should be taken into account when interpreting the absolute values of the deepest part of our model, including our LAB proxy.

Another limitation of our model is that it assumes a radially isotropic Earth. When considering the Australian upper mantle at 75–250 km depth, this assumption is not strictly valid, as demonstrated by previous studies (Debayle & Kennett, 2000b; Fichtner et al., 2010; Kennett et al., 2013; Yoshizawa, 2014). Our choice of retrieving an isotropic V_S model is partly motivated by the findings of Taira and Yoshizawa (2020), who pointed to the limited ability of fundamental-mode surface waves to resolve radial anisotropy beneath Australia. In general, neglecting radial anisotropy simplifies the inverse problem described in Section 5.1, since it considerably increases the ratio of data to model parameters. As mentioned earlier, the inversion of surface-wave velocities for isotropic V_S is challenging due to its non-uniqueness. Simultaneously constraining V_{SV} and V_{SH} based on fundamental modes alone is even more difficult, particularly at relatively large depths, due to the much larger parameter space. This challenge can be addressed by incorporating both fundamental and higher modes (Yoshizawa, 2014), which we plan to investigate in future research.

7. Conclusions

We have derived a 3-D shear-wave velocity model of the Australian crust and upper mantle that extends to 300 km depth. The joint use of seismic ambient noise and teleseismic earthquakes allowed us to fill a tomographic gap in the known shear-wave velocity structure of the continent, comprising lower-crustal to uppermost mantle depths, without resorting to the interpolation of preexisting models. This gap also included continent-wide estimates of Moho depth, of which we provided a surface-wave-based proxy.

In general, the large-scale features of our model are consistent with those reported in AuSREM. Owing to the enhanced seismic coverage available in this study and to the use of state-of-the-art seismic-tomography techniques, however, our model displays higher resolution throughout the crust. At shallow depths (<10 km), shear-velocity variations across Australia highlight known geological domains. While low velocities are found in regions of thick sedimentary layers (as, e.g., in the Canning and Eromanga Basin), high velocities characterize the major cratonic blocks (e.g., Yilgarn, Pilbara, and Gawler Craton). Beneath the large region spanned by the West Australian Craton, such high velocities can be followed through the entire crust and upper mantle, indicating a thickened and cold lithospheric root. In the Tasmanides, the velocity contrast between the fast New England Orogen and the surrounding sedimentary basins is shown in this study at unprecedented resolution.

At greater (upper mantle) depths, similar to AuSREM, the most prominent feature of our model is a large-scale velocity decrease from west to east. This feature translates into LAB depths decreasing eastward, of which we

provided a proxy. The derived proxy essentially suggests that Cainozoic intraplate volcanism in eastern Australia is controlled by lithospheric thickness. Notably, our LAB proxy also features a stripe of thicker lithosphere, extending east to the coast, that has been noticed in previous studies but not visible in AuSREM. As evidenced by the distribution of the volcanic outcrops in Eastern Australia, this observation further supports the hypothesis that lateral variations in lithospheric thickness can lead to a change in both composition and amount of volcanism at the surface.

Data Availability Statement

All shapefiles corresponding to the major geologic units (Figure 1a) were downloaded from Geoscience Australia Portal (https://portal.ga.gov.au/), while the OZ SEEBASE® 2021 model (Figure 1b) from Geognostics (2021). We used publicly available seismic data from the Incorporated Research Institutions for Seismology Data Management Center (https://ds.iris.edu/ds/nodes/dmc/), the Australian Passive Seismic Server (http://auspass.edu.au/), and the EIDA archive (http://www.orfeus-eu.org/eida). The used seismic records are associated with the following network codes: IE (10.7914/SN/1E_2013), 1F (10.7914/SN/1F_2009), 1G (10.7914/SN/1G_2008), 1H (10.7914/SN/1H_2010), 1K (10.7914/SN/1K_2013), 1P (10.7914/SN/1P_2011), 1Q (10.7914/SN/1Q_2016), 3G (10.7914/SN/3G_2018), 4J (10.7914/SN/4J_2014), 5J 10.7914/SN/5J_2017, 6F (10.7914/SN/6F_2008), 7B (https://doi.org/10.7914/SN/7B_1993), 7D (10.7914/SN/7D_1997), 7E (10.7914/SN/7E_1998), 7F (10.7914/SN/7F_1999), 7G (10.7914/SN/7G_2000), 7H (10.7914/SN/7H_2001), 7I (10.7914/SN/7I_2003), 7J (10.7914/SN/7J_2005), 7K (10.7914/SN/7K_2007), 7L (10.7914/SN/7L_2011), 7M (10.7914/SN/7M_2014), 7S (10.7914/SN/7S_2006), 7T (10.7914/SN/7T_2007), 7U (10.7914/SN/7U_2007), 8J (10.7914/SN/8J_2012), 8K (10.7914/SN/8K_2014), AU (10.26186/144675), DU (10.7914/SN/DU), G (10.18715/GEOSCOPE.G), GE (10.14470/TR560404), II (10.7914/SN/II), IU (10.7914/SN/IU), MS (https://www.fdsn.org/networks/detail/MS/), MY (https://www.fdsn.org/networks/detail/MY/), PS (https://www.fdsn.org/networks/detail/PS/), S1 (10.7914/SN/S1), TM (https://www.fdsn.org/networks/detail/TM/), XD (10.7914/SN/XD_2001), XX (10.7914/SN/XX_2013), YS (10.7914/SN/YS_2014), YW (10.7914/SN/YW_2021), ZB (https://www.fdsn.org/networks/detail/ZB_2007/), ZN (10.7914/SN/ZN_2010), ZR (10.7914/SN/ZR_2009).

Acknowledgments
We acknowledge the makers of ObsPy (Beyreuther et al., 2010) and Matplotlib (Hunter, 2007). This work was funded by the Deutsche Forschungsgemeinschaft (DFG—German Research Foundation) under the Individual Research Project: SI 1748/4-1. Open Access funding enabled and organized by Projekt DEAL.

References

Aster, R. C., Borchers, B., & Thurber, C. H. (2018). *Parameter estimation and inverse problems*. Elsevier.
Barley, M., Loader, S., & McNaughton, N. (1998). 3430 to 3417 Ma calc-alkaline volcanism in the McPhee Dome and Kelly Belt, and growth of the eastern Pilbara Craton. *Precambrian Research*, *88*(1–4), 3–23. https://doi.org/10.1016/s0301-9268(97)00061-2
Berteussen, K.-A. (1977). Moho depth determinations based on spectral-ratio analysis of NORSAR long-period P waves. *Physics of the Earth and Planetary Interiors*, *15*(1), 13–27. https://doi.org/10.1016/0031-9201(77)90006-1
Betts, P. G., & Giles, D. (2006). The 1800–1100 Ma tectonic evolution of Australia. *Precambrian Research*, *144*(1–2), 92–125. https://doi.org/10.1016/j.precamres.2005.11.006
Betts, P. G., Giles, D., Lister, G., & Frick, L. (2002). Evolution of the Australian lithosphere. *Australian Journal of Earth Sciences*, *49*(4), 661–695. https://doi.org/10.1046/j.1440-0952.2002.00948.x
Beyreuther, M., Barsch, R., Krischer, L., Megies, T., Behr, Y., & Wassermann, J. (2010). ObsPy: A Python toolbox for seismology. *Seismological Research Letters*, *81*(3), 530–533. https://doi.org/10.1785/gssrl.81.3.530
Birkey, A., Ford, H. A., Dabney, P., & Goldhagen, G. (2021). The lithospheric architecture of Australia from seismic receiver functions. *Journal of Geophysical Research: Solid Earth*, *126*(4), e2020JB020. https://doi.org/10.1029/2020jb020999
Blewett, R. (2012). Shaping a nation: A geology of Australia.
Bodin, T., & Sambridge, M. (2009). Seismic tomography with the reversible jump algorithm. *Geophysical Journal International*, *178*(3), 1411–1436. https://doi.org/10.1111/j.1365-246x.2009.04226.x
Bodin, T., Sambridge, M., Tkalčić, H., Arroucau, P., Gallagher, K., & Rawlinson, N. (2012). Transdimensional inversion of receiver functions and surface wave dispersion. *Journal of Geophysical Research*, *117*(B2). https://doi.org/10.1029/2011jb008560
Boschi, L., & Dziewonski, A. M. (1999). High-and low-resolution images of the Earth's mantle: Implications of different approaches to tomographic modeling. *Journal of Geophysical Research*, *104*(B11), 25567–25594. https://doi.org/10.1029/1999jb900166
Boschi, L., & Weemstra, C. (2015). Stationary-phase integrals in the cross correlation of ambient noise. *Reviews of Geophysics*, *53*(2), 411–451. https://doi.org/10.1002/2014rg000455
Braun, J., Burbidge, D., Gesto, F., Sandiford, M., Gleadow, A. J. W., Kohn, B., & Cummins, P. (2009). Constraints on the current rate of deformation and surface uplift of the Australian continent from a new seismic database and low-T thermochronological data. *Australian Journal of Earth Sciences*, *56*(2), 99–110. https://doi.org/10.1080/08120090802546977
Calò, M., Bodin, T., & Romanowicz, B. (2016). Layered structure in the upper mantle across North America from joint inversion of long and short period seismic data. *Earth and Planetary Science Letters*, *449*, 164–175. https://doi.org/10.1016/j.epsl.2016.05.054
Cawood, P. A., & Tyler, I. M. (2004). Assembling and reactivating the Proterozoic Capricorn Orogen: Lithotectonic elements, orogenies, and significance. *Precambrian Research*, *128*(3–4), 201–218. https://doi.org/10.1016/j.precamres.2003.09.001
Cowley, W. (2020). Geological setting of exceptional geological features of the Flinders Ranges. *Australian Journal of Earth Sciences*, *67*(6), 763–785. https://doi.org/10.1080/08120099.2020.1748109
Crowder, E., Rawlinson, N., Pilia, S., Cornwell, D., & Reading, A. (2019). Transdimensional ambient noise tomography of bass strait, southeast Australia, reveals the sedimentary basin and deep crustal structure beneath a failed continental rift. *Geophysical Journal International*, *217*(2), 970–987. https://doi.org/10.1093/gji/ggz057

Davies, D., Rawlinson, N., Iaffaldano, G., & Campbell, I. H. (2015). Lithospheric controls on magma composition along Earth's longest continental hotspot track. *Nature*, *525*(7570), 511–514. https://doi.org/10.1038/nature14903

Debayle, E., & Kennett, B. (2000a). The Australian continental upper mantle: Structure and deformation inferred from surface waves. *Journal of Geophysical Research*, *105*(B11), 25423–25450. https://doi.org/10.1029/2000jb900212

Debayle, E., & Kennett, B. (2000b). Anisotropy in the Australasian upper mantle from Love and Rayleigh waveform inversion. *Earth and Planetary Science Letters*, *184*(1), 339–351. https://doi.org/10.1016/s0012-821x(00)00314-9

de Vries, S. T., Pryer, L. L., & Fry, N. (2008). Evolution of Neoarchaean and Proterozoic basins of Australia. *Precambrian Research*, *166*(1–4), 39–53. https://doi.org/10.1016/j.precamres.2008.01.005

Direen, N., & Crawford, A. (2003a). The Tasman line: Where is it, what is it, and is it Australia's Rodinian breakup boundary? *Australian Journal of Earth Sciences*, *50*(4), 491–502. https://doi.org/10.1046/j.1440-0952.2003.01005.x

Direen, N. G., & Crawford, A. J. (2003b). Fossil seaward-dipping reflector sequences preserved in southeastern Australia: A 600 Ma volcanic passive margin in eastern Gondwanaland. *Journal of the Geological Society*, *160*(6), 985–990. https://doi.org/10.1144/0016-764903-010

Dreiling, J., & Tilmann, F. (2019). BayHunter-McMC transdimensional Bayesian inversion of receiver functions and surface wave dispersion. Technical report. https://doi.org/10.5880/GFZ.2.4.2019.001

Dziewonski, A. M., & Anderson, D. L. (1981). Preliminary reference Earth model. *Physics of the Earth and Planetary Interiors*, *25*(4), 297–356. https://doi.org/10.1016/0031-9201(81)90046-7

Ekström, G. (2011). A global model of Love and Rayleigh surface wave dispersion and anisotropy, 25-250 s. *Geophysical Journal International*, *187*(3), 1668–1686. https://doi.org/10.1111/j.1365-246x.2011.05225.x

Ekström, G. (2014). Love and Rayleigh phase-velocity maps, 5–40 s, of the western and central USA from USArray data. *Earth and Planetary Science Letters*, *402*, 42–49. https://doi.org/10.1016/j.epsl.2013.11.022

Ekström, G., Abers, G. A., & Webb, S. C. (2009). Determination of surface-wave phase velocities across USArray from noise and Aki's spectral formulation. *Geophysical Research Letters*, *36*(18), L18301. https://doi.org/10.1029/2009gl039131

Ekström, G., Tromp, J., & Larson, E. W. (1997). Measurements and global models of surface wave propagation. *Journal of Geophysical Research*, *102*(B4), 8137–8157. https://doi.org/10.1029/96jb03729

Fichtner, A., Kennett, B. L., Igel, H., & Bunge, H.-P. (2010). Full waveform tomography for radially anisotropic structure: New insights into present and past states of the Australasian upper mantle. *Earth and Planetary Science Letters*, *290*(3–4), 270–280. https://doi.org/10.1016/j.epsl.2009.12.003

Finlayson, D., & Collins, C. (1993). Lithospheric velocity structures under the southern New England Orogen: Evidence for underplating at the Tasman Sea margin. *Australian Journal of Earth Sciences*, *40*(2), 141–153. https://doi.org/10.1080/08120099308728071

Fishwick, S., Heintz, M., Kennett, B., Reading, A., & Yoshizawa, K. (2008). Steps in lithospheric thickness within eastern Australia, evidence from surface wave tomography. *Tectonics*, *27*(4). https://doi.org/10.1029/2007tc002116

Ford, H. A., Fischer, K. M., Abt, D. L., Rychert, C. A., & Elkins-Tanton, L. T. (2010). The lithosphere–asthenosphere boundary and cratonic lithospheric layering beneath Australia from sp wave imaging. *Earth and Planetary Science Letters*, *300*(3–4), 299–310. https://doi.org/10.1016/j.epsl.2010.10.007

Foster, D. A., & Gray, D. R. (2000). Evolution and structure of the Lachlan Fold Belt (Orogen) of eastern Australia. *Annual Review of Earth and Planetary Sciences*, *28*(1), 47–80. https://doi.org/10.1146/annurev.earth.28.1.47

Foti, S., Comina, C., Boiero, D., & Socco, L. (2009). Non-uniqueness in surface-wave inversion and consequences on seismic site response analyses. *Soil Dynamics and Earthquake Engineering*, *29*(6), 982–993. https://doi.org/10.1016/j.soildyn.2008.11.004

Geognostics, OZ SEEBASE® (2021). Geognostics Australia Pty Ltd [Dataset]. https://www.geognostics.com/oz-seebase-2021

Giles, D., Betts, P. G., & Lister, G. S. (2004). 1.8–1.5-Ga links between the north and south Australian cratons and the early–middle Proterozoic configuration of Australia. *Tectonophysics*, *380*(1–2), 27–41. https://doi.org/10.1016/j.tecto.2003.11.010

Glen, R. (2013). Refining accretionary orogen models for the Tasmanides of eastern Australia. *Australian Journal of Earth Sciences*, *60*(3), 315–370. https://doi.org/10.1080/08120099.2013.772537

Glen, R. (2005). *The Tasmanides of eastern Australia* (Vol. 246, p. 23). Special Publication-Geological Society of London.

Glen, R., & Meffre, S. (2009). Styles of Cenozoic collisions in the Western and southwestern Pacific and their applications to Palaeozoic collisions in the Tasmanides of eastern Australia. *Tectonophysics*, *479*(1–2), 130–149. https://doi.org/10.1016/j.tecto.2009.03.023

Gray, D., & Foster, D. (2004). Tectonic evolution of the Lachlan Orogen, southeast Australia: Historical review, data synthesis and modern perspectives. *Australian Journal of Earth Sciences*, *51*(6), 773–817. https://doi.org/10.1111/j.1400-0952.2004.01092.x

Greenfield, T., Gilligan, A., Pilia, S., Cornwell, D. G., Tongkul, F., Widiyantoro, S., & Rawlinson, N. (2022). Post-subduction tectonics of Sabah, Northern Borneo, inferred from surface wave tomography. *Geophysical Research Letters*, *49*(3), e2021GL096. https://doi.org/10.1029/2021gl096117

Hansen, P. C. (1999). The L-curve and its use in the numerical treatment of inverse problems.

Harrison, T., Blichert-Toft, J., Muller, W., Albarede, F., Holden, P., & Mojzsis, S. J. (2005). Heterogeneous Hadean hafnium: Evidence of continental crust at 4.4 to 4.5 Ga. *Science*, *310*(5756), 1947–1950. https://doi.org/10.1126/science.1117926

Haskell, N. A. (1953). The dispersion of surface waves on multilayered media. *Bulletin of the Seismological Society of America*, *43*(1), 17–34. https://doi.org/10.1785/bssa0430010017

Hunter, J. D. (2007). Matplotlib: A 2D graphics environment. *Computing in Science & Engineering*, *9*(03), 90–95. https://doi.org/10.1109/mcse.2007.55

Kästle, E. D., El-Sharkawy, A., Boschi, L., Meier, T., Rosenberg, C., Bellahsen, N., et al. (2018). Surface wave tomography of the Alps using ambient-noise and earthquake phase velocity measurements. *Journal of Geophysical Research: Solid Earth*, *123*(2), 1770–1792. https://doi.org/10.1002/2017jb014698

Kästle, E. D., Soomro, R., Weemstra, C., Boschi, L., & Meier, T. (2016). Two-receiver measurements of phase velocity: Cross-validation of ambient-noise and earthquake-based observations. *Geophysical Journal International*, *207*(3), 1493–1512. https://doi.org/10.1093/gji/ggw341

Kennett, B., Chopping, R., & Blewett, R. (2018). *The Australian continent: A geophysical synthesis*. ANU Press.

Kennett, B., Yoshizawa, K., & Furumura, T. (2017). Interactions of multi-scale heterogeneity in the lithosphere: Australia. *Tectonophysics*, *717*, 193–213. https://doi.org/10.1016/j.tecto.2017.07.009

Kennett, B. L., Fichtner, A., Fishwick, S., & Yoshizawa, K. (2013). Australian seismological reference model (AuSREM): Mantle component. *Geophysical Journal International*, *192*(2), 871–887. https://doi.org/10.1093/gji/ggs065

Kennett, B. L., Fishwick, S., Reading, A. M., & Rawlinson, N. (2004). Contrasts in mantle structure beneath Australia: Relation to Tasman lines? *Australian Journal of Earth Sciences*, *51*(4), 563–569. https://doi.org/10.1111/j.1400-0952.2004.01075.x

Kennett, B. L., Gorbatov, A., Yuan, H., Agrawal, S., Murdie, R., Doublier, M., et al. (2023). Refining the moho across the Australian continent. *Geophysical Journal International*, *223*(3), 1863–1877. https://doi.org/10.1093/gji/ggad035

Korostelev, F., Lu, Y., Magrini, F., Boschi, L., Leroy, S., & Vétel, W. (2022). Images of the East African rift system by global adaptive-resolution surface-wave tomography. *Journal of Geophysical Research: Solid Earth*, *127*(6), e2021JB023. https://doi.org/10.1029/2021jb023570

Lebedev, S., Adam, J. M.-C., & Meier, T. (2013). Mapping the Moho with seismic surface waves: A review, resolution analysis, and recommended inversion strategies. *Tectonophysics*, *609*, 377–394. https://doi.org/10.1016/j.tecto.2012.12.030

Li, G., Yang, Y., Niu, F., & Chen, M. (2021). 3-D sedimentary structures beneath southeastern Australia constrained by passive seismic array data. *Journal of Geophysical Research: Solid Earth*, *126*(2), e2020JB019. https://doi.org/10.1029/2020jb019998

Li, Z.-X., Bogdanova, S., Collins, A., Davidson, A., De Waele, B., Ernst, R., et al. (2008). Assembly, configuration, and break-up history of Rodinia: A synthesis. *Precambrian Research*, *160*(1–2), 179–210. https://doi.org/10.1016/j.precamres.2007.04.021

Lomax, A., & Snieder, R. (1994). Finding sets of acceptable solutions with a genetic algorithm with application to surface wave group dispersion in Europe. *Geophysical Research Letters*, *21*(24), 2617–2620. https://doi.org/10.1029/94gl02635

Magrini, F., & Boschi, L. (2021). Surface-wave attenuation from seismic ambient noise: Numerical validation and application. *Journal of Geophysical Research: Solid Earth*, *126*(1), e2020JB019. https://doi.org/10.1029/2020jb019865

Magrini, F., Diaferia, G., Boschi, L., & Cammarano, F. (2020). Arrival-angle effects on two-receiver measurements of phase velocity. *Geophysical Journal International*, *220*(3), 1838–1844. https://doi.org/10.1093/gji/ggz560

Magrini, F., Diaferia, G., El-Sharkawy, A., Cammarano, F., van der Meijde, M., Meier, T., & Boschi, L. (2022). Surface-wave tomography of the Central-Western Mediterranean: New insights into the Liguro-Provençal and Tyrrhenian Basins. *Journal of Geophysical Research: Solid Earth*, *127*(3), e2021JB023. https://doi.org/10.1029/2021jb023267

Magrini, F., Lauro, S., Kästle, E., & Boschi, L. (2022). Surface-wave tomography using SeisLib: A Python package for multiscale seismic imaging. *Geophysical Journal International*, *231*(2), 1011–1030. https://doi.org/10.1093/gji/ggac236

Meert, J. G. (2001). Growing Gondwana and rethinking Rodinia: A paleomagnetic perspective. *Gondwana Research*, *4*(3), 279–288. https://doi.org/10.1016/s1342-937x(05)70329-4

Meier, T., Dietrich, K., Stöckhert, B., & Harjes, H.-P. (2004). One-dimensional models of shear wave velocity for the eastern Mediterranean obtained from the inversion of Rayleigh wave phase velocities and tectonic implications. *Geophysical Journal International*, *156*(1), 45–58. https://doi.org/10.1111/j.1365-246x.2004.02121.x

Molinari, I., & Morelli, A. (2011). EPcrust: A reference crustal model for the European Plate. *Geophysical Journal International*, *185*(1), 352–364. https://doi.org/10.1111/j.1365-246x.2011.04940.x

Myers, J. S., Shaw, R. D., & Tyler, I. M. (1996). Tectonic evolution of proterozoic Australia. *Tectonics*, *15*(6), 1431–1446. https://doi.org/10.1029/96tc02356

Pilia, S., Rawlinson, N., Cayley, R., Bodin, T., Musgrave, R., Reading, A., et al. (2015a). Evidence of micro-continent entrainment during crustal accretion. *Scientific Reports*, *5*(1), 1–6. https://doi.org/10.1038/srep08218

Pilia, S., Rawlinson, N., Direen, N., Cummins, P. R., & Balfour, N. (2013). Structural controls on localized intraplate deformation and seismicity in Southern Australia: Insights from local earthquake tomography of the Flinders Ranges. *Journal of Geophysical Research: Solid Earth*, *118*(5), 2176–2190. https://doi.org/10.1002/jgrb.50168

Pilia, S., Rawlinson, N., Direen, N., Reading, A. M., Cayley, R., Pryer, L., et al. (2015). Linking mainland Australia and Tasmania using ambient seismic noise tomography: Implications for the tectonic evolution of the east Gondwana margin. *Gondwana Research*, *28*(3), 1212–1227. https://doi.org/10.1016/j.gr.2014.09.014

Powell, C. M., Li, Z.-X., McElhinny, M., Meert, J., & Park, J. (1993). Paleomagnetic constraints on timing of the Neoproterozoic breakup of Rodinia and the Cambrian formation of Gondwana. *Geology*, *21*(10), 889–892. https://doi.org/10.1130/0091-7613(1993)021<0889:pcotot>2.3.co;2

Preiss, W. (2000). The Adelaide Geosyncline of south Australia and its significance in Neoproterozoic continental reconstruction. *Precambrian Research*, *100*(1–3), 21–63. https://doi.org/10.1016/s0301-9268(99)00068-6

Priestley, K., & McKenzie, D. (2006). The thermal structure of the lithosphere from shear wave velocities. *Earth and Planetary Science Letters*, *244*(1–2), 285–301. https://doi.org/10.1016/j.epsl.2006.01.008

Rawlinson, N., Davies, D., & Pilia, S. (2017). The mechanisms underpinning Cenozoic intraplate volcanism in eastern Australia: Insights from seismic tomography and geodynamic modeling. *Geophysical Research Letters*, *44*(19), 9681–9690. https://doi.org/10.1002/2017gl074911

Rawlinson, N., & Kennett, B. (2008). Teleseismic tomography of the upper mantle beneath the southern Lachlan Orogen, Australia. *Physics of the Earth and Planetary Interiors*, *167*(1–2), 84–97. https://doi.org/10.1016/j.pepi.2008.02.007

Rawlinson, N., Pilia, S., Young, M., Salmon, M., & Yang, Y. (2016). Crust and upper mantle structure beneath southeast Australia from ambient noise and teleseismic tomography. *Tectonophysics*, *689*, 143–156. https://doi.org/10.1016/j.tecto.2015.11.034

Rawlinson, N., Pozgay, S., & Fishwick, S. (2010). Seismic tomography: A window into deep Earth. *Physics of the Earth and Planetary Interiors*, *178*(3–4), 101–135. https://doi.org/10.1016/j.pepi.2009.10.002

Rawlinson, N., Reading, A. M., & Kennett, B. L. (2006). Lithospheric structure of Tasmania from a novel form of teleseismic tomography. *Journal of Geophysical Research*, *111*(B2). https://doi.org/10.1029/2005jb003803

Rawlinson, N., Salmon, M., & Kennett, B. L. (2014). Transportable seismic array tomography in southeast Australia: Illuminating the transition from Proterozoic to Phanerozoic lithosphere. *Lithos*, *189*, 65–76. https://doi.org/10.1016/j.lithos.2013.06.001

Rawlinson, N., & Sambridge, M. (2003). Seismic traveltime tomography of the crust and lithosphere. *Advances in Geophysics*, *46*, 81–199.

Roberts, G. G., White, N., Hoggard, M. J., Ball, P. W., & Meenan, C. (2018). A Neogene history of mantle convective support beneath Borneo. *Earth and Planetary Science Letters*, *496*, 142–158. https://doi.org/10.1016/j.epsl.2018.05.043

Rosenbaum, G. (2018). The tasmanides: Phanerozoic tectonic evolution of eastern Australia. *Annual Review of Earth and Planetary Sciences*, *46*(1), 291–325. https://doi.org/10.1146/annurev-earth-082517-010146

Salmon, M., Kennett, B., & Saygin, E. (2013). Australian seismological reference model (AuSREM): Crustal component. *Geophysical Journal International*, *192*(1), 190–206. https://doi.org/10.1093/gji/ggs004

Sambridge, M. (1999). Geophysical inversion with a neighbourhood algorithm—I. Searching a parameter space. *Geophysical Journal International*, *138*(2), 479–494. https://doi.org/10.1046/j.1365-246x.1999.00876.x

Sambridge, M., Gallagher, K., Jackson, A., & Rickwood, P. (2006). Trans-dimensional inverse problems, model comparison and the evidence. *Geophysical Journal International*, *167*(2), 528–542. https://doi.org/10.1111/j.1365-246x.2006.03155.x

Sambridge, M., & Mosegaard, K. (2002). Monte Carlo methods in geophysical inverse problems. *Reviews of Geophysics*, *40*(3), 3–1. https://doi.org/10.1029/2000rg000089

Sandiford, M., Leonard, M., & Coblentz, D. (2003). Geological constraints on active seismicity in southeast Australia. *Earthquake Risk Mitigation*, 1–10.

Saygin, E., & Kennett, B. (2012). Crustal structure of Australia from ambient seismic noise tomography. *Journal of Geophysical Research*, *117*(B1). https://doi.org/10.1029/2011jb008403

Saygin, E., & Kennett, B. L. (2010). Ambient seismic noise tomography of Australian continent. *Tectonophysics*, *481*(1–4), 116–125. https://doi.org/10.1016/j.tecto.2008.11.013

Seats, K. J., Lawrence, J. F., & Prieto, G. A. (2012). Improved ambient noise correlation functions using Welch's method. *Geophysical Journal International*, *188*(2), 513–523. https://doi.org/10.1111/j.1365-246x.2011.05263.x

Smith, D. B., Ritzwoller, M. H., & Shapiro, N. M. (2004). Stratification of anisotropy in the Pacific upper mantle. *Journal of Geophysical Research*, *109*(B11). https://doi.org/10.1029/2004jb003200

Soomro, R., Weidle, C., Cristiano, L., Lebedev, S., Meier, T., & Group, P. W. (2016). Phase velocities of Rayleigh and Love waves in central and northern Europe from automated, broad-band, interstation measurements. *Geophysical Journal International*, *204*(1), 517–534. https://doi.org/10.1093/gji/ggv462

Spampinato, G. P., Betts, P. G., Ailleres, L., & Armit, R. J. (2015). Early tectonic evolution of the Thomson Orogen in Queensland inferred from constrained magnetic and gravity data. *Tectonophysics*, *651*, 99–120. https://doi.org/10.1016/j.tecto.2015.03.016

Sun, W., & Kennett, B. (2016). Uppermost mantle structure of the Australian continent from Pn traveltime tomography. *Journal of Geophysical Research: Solid Earth*, *121*(3), 2004–2019. https://doi.org/10.1002/2015jb012597

Sun, W., Kennett, B., Zhao, L., & Fu, L.-Y. (2018). Continental lithospheric layering beneath stable, modified, and destroyed cratons from seismic daylight imaging. *Lithospheric discontinuities*, (pp. 155–176).

Taira, T., & Yoshizawa, K. (2020). Upper-mantle discontinuities beneath Australia from transdimensional Bayesian inversions using multimode surface waves and receiver functions. *Geophysical Journal International*, *223*(3), 2085–2100. https://doi.org/10.1093/gji/ggaa442

Thomson, W. T. (1950). Transmission of elastic waves through a stratified solid medium. *Journal of Applied Physics*, *21*(2), 89–93. https://doi.org/10.1063/1.1699629

Trefethen, L. N., & Bau, D. (1997). *Numerical linear algebra* (Vol. 50). SIAM.

Valley, J. W., Cavosie, A. J., Ushikubo, T., Reinhard, D. A., Lawrence, D. F., Larson, D. J., et al. (2014). Hadean age for a post-magma-ocean zircon confirmed by atom-probe tomography. *Nature Geoscience*, *7*(3), 219–223. https://doi.org/10.1038/ngeo2075

van der Hilst, R., Kennett, B., Christie, D., & Grant, J. (1994). Project Skippy explores lithosphere and mantle beneath Australia. *EOS, Transactions American Geophysical Union*, *75*(15), 177–181. https://doi.org/10.1029/94eo00857

Wade, B., Kelsey, D., Hand, M., & Barovich, K. (2008). The Musgrave Province: Stitching north, west and south Australia. *Precambrian Research*, *166*(1–4), 370–386. https://doi.org/10.1016/j.precamres.2007.05.007

Walter, M., Veevers, J., Calver, C., & Grey, K. (1995). Neoproterozoic stratigraphy of the Centralian superbasin, Australia. *Precambrian Research*, *73*(1–4), 173–195. https://doi.org/10.1016/0301-9268(94)00077-5

Wathelet, M. (2005). *Array recordings of ambient vibrations: Surface-wave inversion*, (Vol. 161). PhD Diss. Liége University.

Wathelet, M. (2008). An improved neighborhood algorithm: Parameter conditions and dynamic scaling. *Geophysical Research Letters*, *35*(9), L09301. https://doi.org/10.1029/2008gl033256

Wingate, M. T., Campbell, I. H., Compston, W., & Gibson, G. M. (1998). Ion microprobe U–Pb ages for Neoproterozoic basaltic magmatism in south-central Australia and implications for the breakup of Rodinia. *Precambrian Research*, *87*(3–4), 135–159. https://doi.org/10.1016/s0301-9268(97)00072-7

Wingate, M. T., & Giddings, J. W. (2000). Age and palaeomagnetism of the Mundine well dyke swarm, Western Australia: Implications for an Australia–Laurentia connection at 755 Ma. *Precambrian Research*, *100*(1–3), 335–357. https://doi.org/10.1016/s0301-9268(99)00080-7

Yang, Y., Li, A., & Ritzwoller, M. H. (2008). Crustal and uppermost mantle structure in southern Africa revealed from ambient noise and teleseismic tomography. *Geophysical Journal International*, *174*(1), 235–248. https://doi.org/10.1111/j.1365-246x.2008.03779.x

Yoshizawa, K. (2014). Radially anisotropic 3-D shear wave structure of the Australian lithosphere and asthenosphere from multi-mode surface waves. *Physics of the Earth and Planetary Interiors*, *235*, 33–48. https://doi.org/10.1016/j.pepi.2014.07.008

Yoshizawa, K., & Kennett, B. (2004). Multimode surface wave tomography for the Australian region using a three-stage approach incorporating finite frequency effects. *Journal of Geophysical Research*, *109*(B2). https://doi.org/10.1029/2002jb002254

Yoshizawa, K., & Kennett, B. (2015). The lithosphere-asthenosphere transition and radial anisotropy beneath the Australian continent. *Geophysical Research Letters*, *42*(10), 3839–3846. https://doi.org/10.1002/2015gl063845

Young, M., Cayley, R., McLean, M., Rawlinson, N., Arroucau, P., & Salmon, M. (2013). Crustal structure of the east gondwana margin in southeast Australia revealed by transdimensional ambient seismic noise tomography. *Geophysical Research Letters*, *40*(16), 4266–4271. https://doi.org/10.1002/grl.50878

Yuan, H., & Bodin, T. (2018). A probabilistic shear wave velocity model of the crust in the central west Australian craton constrained by transdimensional inversion of ambient noise dispersion. *Tectonics*, *37*(7), 1994–2012. https://doi.org/10.1029/2017tc004834

Zhou, L., Xie, J., Shen, W., Zheng, Y., Yang, Y., Shi, H., & Ritzwoller, M. H. (2012). The structure of the crust and uppermost mantle beneath South China from ambient noise and earthquake tomography. *Geophysical Journal International*, *189*(3), 1565–1583. https://doi.org/10.1111/j.1365-246x.2012.05423.x

Zielhuis, A., & van der Hilst, R. D. (1996). Upper-mantle shear velocity beneath eastern Australia from inversion of waveforms from SKIPPY portable arrays. *Geophysical Journal International*, *127*(1), 1–16. https://doi.org/10.1111/j.1365-246x.1996.tb01530.x